Compositional Effects on Nickel-Base Superalloy Single Crystal Microstructures

Rebecca A. MacKay and Timothy P. Gabb
Glenn Research Center, Cleveland, Ohio

Anita Garg
University of Toledo, Toledo, Ohio

Richard B. Rogers and Michael V. Nathal
Glenn Research Center, Cleveland, Ohio

NASA STI Program . . . in Profile

Since its founding, NASA has been dedicated to the advancement of aeronautics and space science. The NASA Scientific and Technical Information (STI) program plays a key part in helping NASA maintain this important role.

The NASA STI Program operates under the auspices of the Agency Chief Information Officer. It collects, organizes, provides for archiving, and disseminates NASA's STI. The NASA STI program provides access to the NASA Aeronautics and Space Database and its public interface, the NASA Technical Reports Server, thus providing one of the largest collections of aeronautical and space science STI in the world. Results are published in both non-NASA channels and by NASA in the NASA STI Report Series, which includes the following report types:
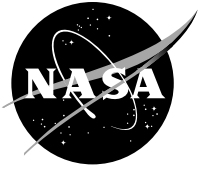
- TECHNICAL PUBLICATION. Reports of completed research or a major significant phase of research that present the results of NASA programs and include extensive data or theoretical analysis. Includes compilations of significant scientific and technical data and information deemed to be of continuing reference value. NASA counterpart of peer-reviewed formal professional papers but has less stringent limitations on manuscript length and extent of graphic presentations.

- TECHNICAL MEMORANDUM. Scientific and technical findings that are preliminary or of specialized interest, e.g., quick release reports, working papers, and bibliographies that contain minimal annotation. Does not contain extensive analysis.

- CONTRACTOR REPORT. Scientific and technical findings by NASA-sponsored contractors and grantees.

- CONFERENCE PUBLICATION. Collected papers from scientific and technical conferences, symposia, seminars, or other meetings sponsored or cosponsored by NASA.

- SPECIAL PUBLICATION. Scientific, technical, or historical information from NASA programs, projects, and missions, often concerned with subjects having substantial public interest.

- TECHNICAL TRANSLATION. English-language translations of foreign scientific and technical material pertinent to NASA's mission.

Specialized services also include creating custom thesauri, building customized databases, organizing and publishing research results.

For more information about the NASA STI program, see the following:

- Access the NASA STI program home page at *http://www.sti.nasa.gov*

- E-mail your question to *help@sti.nasa.gov*

- Fax your question to the NASA STI Information Desk at 443–757–5803

- Phone the NASA STI Information Desk at 443–757–5802

- Write to:
  STI Information Desk
  NASA Center for AeroSpace Information
  7115 Standard Drive
  Hanover, MD 21076–1320

Compositional Effects on Nickel-Base Superalloy Single Crystal Microstructures

Rebecca A. MacKay and Timothy P. Gabb
Glenn Research Center, Cleveland, Ohio

Anita Garg
University of Toledo, Toledo, Ohio

Richard B. Rogers and Michael V. Nathal
Glenn Research Center, Cleveland, Ohio

Acknowledgments

Level of Review: This material has been technically reviewed by expert reviewer(s).

Compositional Effects on Nickel-Base Superalloy Single Crystal Microstructures

Rebecca A. MacKay and Timothy P. Gabb
National Aeronautics and Space Administration
Glenn Research Center
Cleveland, Ohio 44135

Anita Garg
University of Toledo
Toledo, Ohio 43606

Richard B. Rogers and Michael V. Nathal
National Aeronautics and Space Administration
Glenn Research Center
Cleveland, Ohio 44135

Summary

Fourteen nickel-base superalloy single crystals containing 0 to 5 wt% chromium (Cr), 0 to 11 wt% cobalt (Co), 6 to 12 wt% molybdenum (Mo), 0 to 4 wt% rhenium (Re), and fixed amounts of aluminum (Al) and tantalum (Ta) were examined to determine the effect of bulk composition on basic microstructural parameters, including γ' solvus, γ' volume fraction, volume fraction of topologically close-packed (TCP) phases, phase chemistries, and γ-γ' lattice mismatch. Regression models were developed to describe the influence of bulk alloy composition on the microstructural parameters and were compared to predictions by a commercially available software tool that used computational thermodynamics. Co produced the largest change in γ' solvus over the wide compositional range used in this study, and Mo produced the largest effect on the γ lattice parameter and the γ-γ' lattice mismatch over its compositional range, although Re had a very potent influence on all microstructural parameters investigated. Changing the Cr, Co, Mo, and Re contents in the bulk alloy had a significant impact on their concentrations in the γ matrix and, to a smaller extent, in the γ' phase. The γ phase chemistries exhibited strong temperature dependencies that were influenced by the γ and γ' volume fractions. A computational thermodynamic modeling tool significantly underpredicted γ' solvus temperatures and grossly overpredicted the amount of TCP phase at 982 °C. Furthermore, the predictions by the software tool for the γ-γ' lattice mismatch were typically of the wrong sign and magnitude, but predictions could be improved if TCP formation was suspended within the software program. However, the statistical regression models provided excellent estimations of the microstructural parameters based on bulk alloy composition, thereby demonstrating their usefulness.

Introduction

A series of nickel (Ni)-base superalloy single crystals was developed recently (Refs. 1 to 3) in a new compositional design space for potential turbine blade applications. This alloy series, termed low-density single crystal (LDS), was explored in an effort to produce single crystal alloys with low densities while concurrently achieving improved high-temperature creep resistance, microstructural stability, and excellent oxidation resistance. These LDS alloys offer reduced weight, lower fuel burn, and lower emissions for future subsonic aircraft engines.

The Ni-base alloy series developed contained fixed aluminum (Al) and tantalum (Ta) contents for γ' precipitation, as well as variations in the chromium (Cr), cobalt (Co), molybdenum (Mo), and rhenium (Re) contents. Cr was added to the alloy for improved oxidation resistance and was explored (Refs. 1 to 3) at relatively low levels to determine the minimum Cr concentrations required for sufficient oxidation resistance. Co was chosen as a conventional superalloy addition because its density matches that of Ni and, as a result, does not increase alloy density. Co has also been reported to improve alloy stability (Refs. 4 to 7). However, the key alloying strategy employed in this work involved replacing some of the high-density Re, and all of the high-density tungsten (W), with Mo for solid solution strengthening. Mo is a potent solid solution strengthener but has a density almost half that of either Re or W.

The alloys investigated in this report represent the compositional design space described above, which is considered to be novel because of the relatively high Mo content combined with a low Cr content in single crystal form. Superalloy single crystals with high Mo contents were studied earlier (Refs. 8 to 10) in model alloys that were cast without Cr, Co, and Re, in order to investigate systematically the

effects of lattice mismatch on γ′ coarsening and creep behavior in simple model alloys. Other investigations examined the use of higher Mo contents (Refs. 11 to 13), as well as a range of Co (Refs. 4 and 5), but these alloys did not contain Re and tended to have higher Cr levels. More recent studies (Refs. 6, 7, and 14) examined the effect of Re on various microstructural features. However, these alloys did not contain high Mo contents and included W, ruthenium (Ru), and titanium (Ti) along with a number of other significant alloying differences.

The purpose of this report is to characterize more fully the key microstructural parameters that are known to influence the mechanical properties of Ni-base superalloy single crystals. The report focuses on the effects of alloy composition on microstructural parameters, including γ′ solvus, γ′ volume fraction, volume fraction of topologically close-packed (TCP) phases, γ and γ′ phase chemistries, and γ-γ′ lattice mismatch. This report provides quantitative assessments of these microstructural features and regression models that were developed to estimate these microstructural parameters from bulk alloy composition. Ultimately, the microstructural parameters will be used in the development of a creep model that will be described in a future paper. It is expected that the regression models presented herein, coupled with a creep model, will enable the alloy composition to be fine tuned to obtain microstructural features that deliver targeted mechanical properties. Thus, this report will improve the ability for further alloy optimization and will provide additional data needed by potential customers.

Computational thermodynamic modeling tools that are based on the calculation of phase diagrams have been commonly applied to multicomponent Ni-base superalloys. A commercially available software package JMatPro 6.0 (Sente Software Ltd.), which is an acronym for Java-based Materials Properties (Refs. 15 and 16), was employed in this study to predict the microstructural parameters observed experimentally. Thus, the second purpose of this report is to provide additional experimental data for thermodynamic modelers to use to improve the predictive capabilities of these physics-based computational tools for superalloy compositions. It is hoped that the experimental data and interpretation provided here will enable such improvements to occur.

Materials and Experimental Procedures

A design of experiments approach (Refs. 2 and 3) was employed that minimized the number of alloys that needed to be cast. Based on this approach, 14 LDS alloys (Table I) were cast into single crystal slabs at a commercial casting vendor, PCC Airfoils LLC, Minerva, Ohio. The targeted baseline alloy selected for this design strategy contained 6.1 wt% Al, 6.2 wt% Ta, 50 to 100 ppm wt% yttrium (Y), and a balance of Ni. Alloying elements were varied as follows: 0 to 5 wt% Cr; 0 to 11 wt% Co; 6 to 12 wt% Mo; and 0 to 4 wt% Re. These element ranges were chosen (Refs. 2 and 3) to allow for good

predictive capabilities within the compositional design space, thereby enabling potentially attractive alloys for future applications to be defined and explored. Small quantities of carbon (C) and boron (B) were added as grain boundary strengthening elements, which is an approach used more recently in third and fourth generation alloys to reduce the impact of undesirable grain boundary defects (Refs. 2 and 3) that may be present in turbine blades and to improve superalloy cleanliness (Ref. 17). Hafnium (Hf) was added to selected alloys at a nominal level of 0.2 wt% for oxidation resistance.

The slab castings measured approximately 15 cm long in the single crystal growth direction, 5 cm wide, and 0.6 cm thick. The castings were solution treated at a commercial heat treatment vendor. The solution temperature was reached by a series of step increments to avoid incipient melting and overshooting. Single crystal castings without Hf additions were solution treated for 6 h at 1315 °C, and castings with Hf were solution treated for 6 h at 1305 °C. Because of its lower solidus, LDS–1110 was given a step heat treatment with a solution temperature of 1288 °C for 18 h at the NASA Glenn Research Center. All castings were fan quenched in argon (Ar) from the solution temperature to below 1093 °C at a rate of 43 °C/min.

Bulk chemical analyses were performed by inductively coupled plasma emission spectroscopy (ICP) at the top and bottom sections of at least one casting of each composition. In addition, trace impurity levels of sulfur (S) were analyzed in selected alloys by Glow-Discharge Mass Spectroscopy at SHIVA Technologies, Syracuse, New York. Pins, nominally 1.6 mm square by 19 mm long, were supplied for this latter analysis.

Differential Thermal Analysis (DTA) was conducted on LDS alloys in a helium atmosphere using a Netzsch STA 409C instrument. Selected alloys were examined in the as-cast condition, and all alloys were analyzed in the as-solutioned condition. The 1500-mg single crystal samples were heated in a high-purity alumina crucible at a rate of 10 °C/min, from 20 °C through the entire melting range to a maximum temperature of 1500 °C. The helium flow rate was 40 ml/min. Cooling curves were generated from 1500 °C through the same temperature range, also at a rate of 10 °C/min. Liquidus, solidus, and γ′ solvus temperatures were determined from the intersections of tangential lines at the beginning of each transformation in the thermograms of the heating curves.

The γ′ area fractions for each alloy were determined using gauge length sections of tested creep rupture specimens. Longitudinal sections were polished and etched with 33 vol% acetic acid, 33 vol% water, 33 vol% nitric acid, and 1 vol% hydrofluoric acid. Scanning electron microscopy was used in the secondary electron imaging mode to obtain a minimum of five areas at a magnification of ´5000 for each creep rupture specimen examined. Fovea Pro 4.0 imaging software was used to quantify the area fractions of γ′

TABLE I.—ANALYZED COMPOSITIONS OF SINGLE CRYSTAL ALLOYS

Alloy	Content, wt%											
	Cr	Co	Mo	Re	Al	Ta	Hf	Y, Top / Bottom	Ni	B	C	S, ppm wt%
LDS–0010	0.00	0.00	12.02	0.00	6.08	6.14	0.00	0.0053 / 0.0277	75.6	0.0040	0.0140	(a)
LDS–0101	0.01	9.76	7.01	2.92	6.01	6.28	0.00	0.0070 / 0.0180	67.9	0.0045	0.0098	(a)
LDS–5051	2.35	0.00	9.01	2.99	6.03	6.11	0.00	0.0065 / 0.0174	73.4	0.0040	0.0140	2.8
LDS–5555	2.43	4.91	9.48	1.48	6.03	6.17	0.00	0.0046 / 0.0187	69.4	0.0032	0.0168	2.8
LDS–4583	3.90	5.00	8.10	3.00	6.00	6.30	0.21	0.0057 / 0.0067	67.3	0.0030	0.0104	2.8
LDS–4183	3.93	9.97	8.13	3.04	6.05	6.22	0.20	0.0073 / 0.0069	62.4	0.0030	0.0139	3.2
LDS–4164	4.00	11.00	6.10	4.10	6.00	6.20	0.19	0.0073 / 0.0114	62.4	0.0040	0.0110	(a)
LDS–1000	4.79	0.00	7.08	0.00	6.04	6.21	0.00	0.0048 / 0.0210	75.8	0.0030	0.0098	3.1
LDS–1501	4.93	4.98	7.13	3.05	6.01	6.26	0.19	0.0057/ 0.0118	67.4	0.0030	0.0098	(a)
LDS–1101	4.70	9.90	7.10	3.00	6.00	6.20	0.00	0.0050 / 0.0193	63.1	0.0035	0.0160	4.1
LDS–1164	4.90	10.00	6.10	4.00	6.00	6.30	0.19	0.0042 / 0.0084	62.5	0.0030	0.0130	(a)
LDS–1101+Hf	5.00	10.00	7.30	3.10	6.10	6.50	0.19	0.0079 / 0.0076	61.7	(a)	0.0240	0.87
LDS–1182	4.88	9.99	8.19	2.03	5.99	6.25	0.22	0.0066 / 0.0044	62.4	0.0040	0.0097	(a)
LDS–1110	4.68	9.76	11.95	0.00	5.98	6.08	0.00	0.0047 / 0.0177	61.4	0.0030	0.0180	(a)

[a]Not measured.

For determining the area fraction of third phase precipitates in the LDS alloys, transverse cross sections from the uniform gauge length of tested creep rupture specimens were polished metallographically and examined in the unetched condition using back-scattered electron (BSE) microscopy. The third phases that were enriched with heavier elements appeared bright with BSE microscopy and were easily distinguishable from the darker background containing the γ and γ′ phases. BSE images were obtained from a minimum of five locations at magnifications of ´100, ´250, and ´500 in each creep rupture specimen examined, and quantitative image analysis software was employed to determine the area fraction of the third phase precipitates. This technique was also used to measure carbide area fractions in the as-solutioned condition. Energy dispersive spectroscopy (EDS) was used to identify carbide and TCP phase chemistries.

Electrolytic phase extraction was performed on the LDS alloys using standard procedures (Refs. 4 and 18) in order to separate the γ′ precipitates, as well as the carbides and TCP phases, from the γ matrix. The carbides and TCP phases were extracted using an electrolyte of 1 wt% tartaric acid in a solution of 10 vol% hydrochloric acid and 90 vol% methanol. X-ray diffraction of the extracted carbides and TCP phases was used to determine their crystal structures. The γ′ precipitates were extracted in three separate runs with an electrolyte of 1 wt% citric acid and 1 wt% ammonium sulfate in water. After each separate extraction run, the γ′ residue was analyzed by ICP, as was the residual liquor from extraction, which was assumed to represent the γ matrix.

Measurements of γ-γ′ lattice mismatch were performed in situ using a Phillips HR–2 x-ray diffractometer on single crystals that had been aged under the following conditions: 1149 °C for 24 h + 1079 °C for 8 h + 871 °C for 12 h, which was followed by an Ar gas quench to room temperature. The diffractometer had a three-axis goniometer and an incident beam monochromator that passed only the Cu K_{a1} wave-

length. Each sample was aligned after mounting on the diffractometer by iteratively optimizing the w, $2q$, and tilt axes until the difference between the intensity peak and actual position for each axis was less than 0.05°. Data were gathered from the $(400)_{g, g¢}$ peaks, and peak positions were obtained with analytical fitting functions including the Split Pearson VII and the Pearson VII functions.

Regression models for estimating the microstructural parameters were developed using JMP 7.0 (SAS Institute Inc.) by comparing stepwise forward and reverse selection of significant terms, with at least a 90% probability of significance necessary for inclusion of a term. This method allowed for the determination of the influence of specific elements, as well as their interaction terms, on various microstructural parameters. Goodness of fit was assessed using the coefficient of determination adjusted for the number of variables, R^2_{adj}. Residual error in each fitted response was estimated using the root mean square of error (rmsE).

Regression model estimates were compared with the JMatPro-Ni 6.0 predictions of the microstructural parameters. Within this materials property simulation program, the upper and lower heat treatment limits of 1371 and 871 °C, respectively, were selected for allowing phase equilibrium; the phase distributions were frozen below 871 °C. Unless otherwise noted, all phases were taken into account by the simulation program and were allowed to form. The Ni-base superalloy database and the single crystal database, both available with JMatPro-Ni 6.0, were found to provide equivalent predictions.

Experimental Results

Chemical Analyses

Table I shows the analyzed chemistries of the LDS slab castings. The compositions shown are averages of the ICP measurements obtained from the top and bottom sections of the 15-cm-long slabs. The variation in the analyzed contents of the main elements from the top to the bottom of the castings was typically less than 0.1 wt%, with no obvious trends in the main elements as a function of location within the slab. The mean analyzed chemistries were within 0.3 wt% of the desired composition for each main element, but more typically within 0.1 wt% of the desired composition. Thus, there was no particular difficulty in obtaining the chemistry targets for this alloy composition space.

The analyzed levels of the interstitial elements, B, C, nitrogen (N), and oxygen (O), were also within acceptable limits. B and C were intentionally added at very low levels. B has been observed to combine with Cr or Mo to form borides (Ref. 19), and C may combine with Ta or Mo to form carbides. Borides and carbides are known grain boundary strengtheners that can precipitate on undesirable grain boundaries that sometimes form in single crystal castings, and adding these interstitial elements in very small quantities has

become a fairly standard practice in advanced single crystal alloys.

Reactive Y was intentionally added to the alloy design space because of its well-known effect of gettering the S impurity through sulfide formation, thus providing improved oxidation resistance. S was typically measured to be 3 ppm wt% in these castings (Table I). Considerable effort has been expended by superalloy manufacturers to reduce the S impurity in superalloy melts to levels below 10 to 20 ppm wt% (Ref. 19), and it should be noted that the LDS alloys had measured S contents nearly an order of magnitude lower than this limit. However, the retained Y content was observed to vary significantly from top to bottom in many of the single crystal castings. The reason for this variation is that Y can react with the common shell molds used to cast superalloys, so obtaining the targeted level of retained Y can be a challenge. It is evident in Table I that the top sections of the single crystal castings consistently possessed Y contents in a desirable range between 0.0040 and 0.0080 wt%. However, the bottom sections of the slabs were often enriched in Y at levels significantly above the desired maximum of 0.01 wt%. The enrichment in Y was sometimes observed to have caused a small amount (<0.6 vol%) of incipient melting in the bottom casting sections during solutioning, as evidenced by Y-rich precipitates in a spheroidal morphology and associated pores present in low quantities in the bottom sections. Less than 1 vol% of incipient melting is generally considered to be acceptable by industry standards. Nevertheless, in this study, only the top half of each slab was used, in an effort to restrict the retained Y content to an acceptable range and to eliminate incipient melting from samples.

Differential Thermal Analysis

DTA was performed on selected alloys in the as-cast condition and on all alloys in the as-solutioned condition. The thermograms from DTA of the as-cast samples exhibited more gradual transitions through transformations, particularly through the $g¢$ solvus reaction, than did the as-solutioned samples. This difference between the as-cast and as-solutioned materials is likely the result of dendritic segregation effects. Other investigators (Ref. 20) have used heat-treated samples to enhance the detection of the $g¢$ reaction during DTA. In the present study, as-cast samples exhibited $g¢$ solvus temperatures that were up to 5 °C lower and solidus and liquidus temperatures that were up to 12 °C higher than as-solutioned material. This difference was consistent with work previously reported (Ref. 21). The DTA results described in the following paragraphs focus primarily on results obtained from as-solutioned samples because it is in this more homogeneous condition that the material will be used.

In the present study, single crystal samples were heated through the full melting range to a maximum temperature of 1500 °C, and cooling curves were subsequently obtained.

Because the samples were brought through melting, the material, on cooling, had an as-cast structure. Thus, γ¢ solvus, solidus, and liquidus temperatures were obtained from the heating curves only. Duplicate, as-solutioned samples showed consistent results and exhibited solvus, solidus, and liquidus temperatures within 2 °C from sample to sample. Figure 1 shows the γ¢ solvus, solidus, and liquidus temperatures for the LDS alloys as a function of Co content. Co is well known to have a strong effect on reducing γ¢ solvus (Refs. 4 to 6 and 14), and the figure demonstrates that the γ¢ solvus decreased by nearly 50 °C as the Co content was increased from 0 to 11 wt%. The difference between the γ¢ solvus and the solidus is considered to be the solution heat treatment "window." As seen in Figure 1, these alloys typically had at least a 50 °C solution heat treatment window. Microscopy confirmed that all alloys were completely solutioned by the chosen heat treatments.

In addition to the significant effect of Co on γ¢ solvus, refractory metals are known to influence the γ¢ solvus (Refs. 4, 5, 11, and 14) as well. Because the alloy composition matrix was based on a statistical design, more than one element was varied simultaneously in each alloy, and this made it difficult to discern compositional trends with simple x-y scatter plots. As a result, multiple regression was used to determine the effects of alloy composition on the key microstructural parameters. The linear regression model developed for the measured γ¢ solvus and the analyzed bulk chemistries of the elements that were varied in the alloys was the following:

$$\gamma\text{¢ solvus} = 1279.03 - \mathbf{11.69}\ \text{Cr¢} - \mathbf{23.11}\ \text{Co¢} + \mathbf{4.52}\ \text{Mo¢} + \mathbf{9.59}\ \text{Re¢}$$

with R^2_{adj} = 98.6% and rmsE = 2.48 °C   (1)

where the γ¢ solvus is in degrees Celsius. The terms with prime marks in Equation (1) represent the normalized form of each significant element, which is defined as the difference between the analyzed element content and the midpoint of the range of
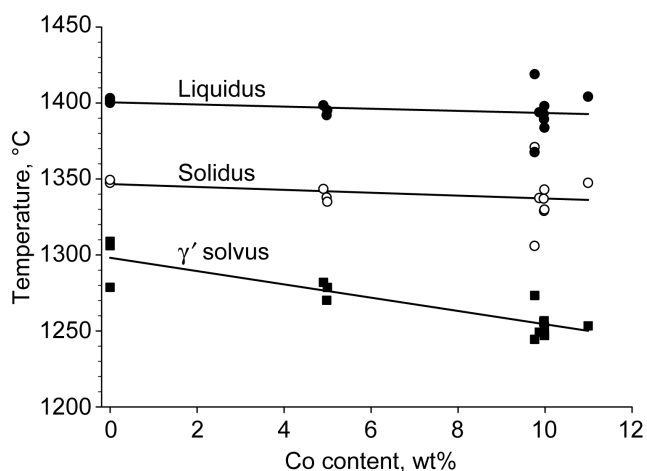

Figure 1.—Differential Thermal Analysis results as a function of bulk Co content.

that element divided by the half-range of that element, all in weight percent. Therefore, Cr¢ = [(Cr – 2.5)/ 2.5], Co¢ = [(Co – 5.5)/5.5], Mo¢ = [(Mo – 9.06)/2.96], and Re¢ = [(Re – 2.05)/2.05]. This approach standardizes each elemental variable to a normalized range of –1 to +1 and allows the relative effect of each element term to be ranked over its entire compositional range according to the magnitude of its coefficient shown in **bold** font in the equation. It should be noted that regression models were also developed for the γ¢ solvus using analyzed compositions in atomic percent, and no significant differences were observed with respect to either the specific terms included in the model or the goodness of fit.

From the magnitude and sign of the regression coefficients in Equation (1), it may be seen that Co and Cr had the most significant effects over their full compositional ranges on the γ¢ solvus, and both of these elements reduced the solvus temperature. This trend was in agreement with other investigations that noted that Co (Refs. 4 to 6 and 14) and Cr (Ref. 14) were γ¢ solvus depressants. Re and Mo raised the solvus but at a smaller magnitude over the compositional ranges used. These compositional effects on the γ¢ solvus are also readily apparent in the regression model output curves in Figures 2(a) to (c), where the estimated solvus temperatures are displayed as a function of Mo content for minimum, midrange, and maximum levels of Cr, Co, and Re, respectively. Figure 2(a) shows the significance of the Cr addition, where increasing the Cr content over the full range used in this study decreased the γ¢ solvus by 23 °C at a constant Mo content with Co and Re held constant at their midrange levels. The very significant impact of Co is depicted in Figure 2(b) by the large displacement between the parallel curves. Here, increasing the Co content from 0 to 11 wt% decreased the γ¢ solvus by 46 °C at a constant Mo content, whereas increasing the Mo content from 6 to 12 wt% at a constant Co content increased the γ¢ solvus by only 9 °C. The model output plot in Figure 2(c) shows that increasing the Re content from 0 to 4 wt% increased the γ¢ solvus by 19 °C at a constant Mo content with Co and Cr at their midrange levels.

The excellent agreement between the measured γ¢ solvus and the γ¢ solvus estimated by the regression equation in Equation (1) is shown in Table II and by the solid symbols in Figure 3. Thus, the scatter evident in Figure 1, particularly at the high Co content, can be attributed to the other compositional variations. Predictions of γ¢ solvus were also obtained from JMatPro 6.0, and these are represented by the open symbols in Figure 3 and are included in Table II. It is evident in the figure and in Table II that JMatPro consistently underpredicted the measured γ¢ solvus; JMatPro solvus predictions were on average 10 °C lower than those determined experimentally. In addition, the higher degree of scatter for the JMatPro predictions indicates that the software was less accurate in predicting absolute values as well as alloy trends. JMatPro also had difficulty predicting the solidus in these alloys since the predicted solidus temperatures were an average of 17 °C lower than the experimental values.
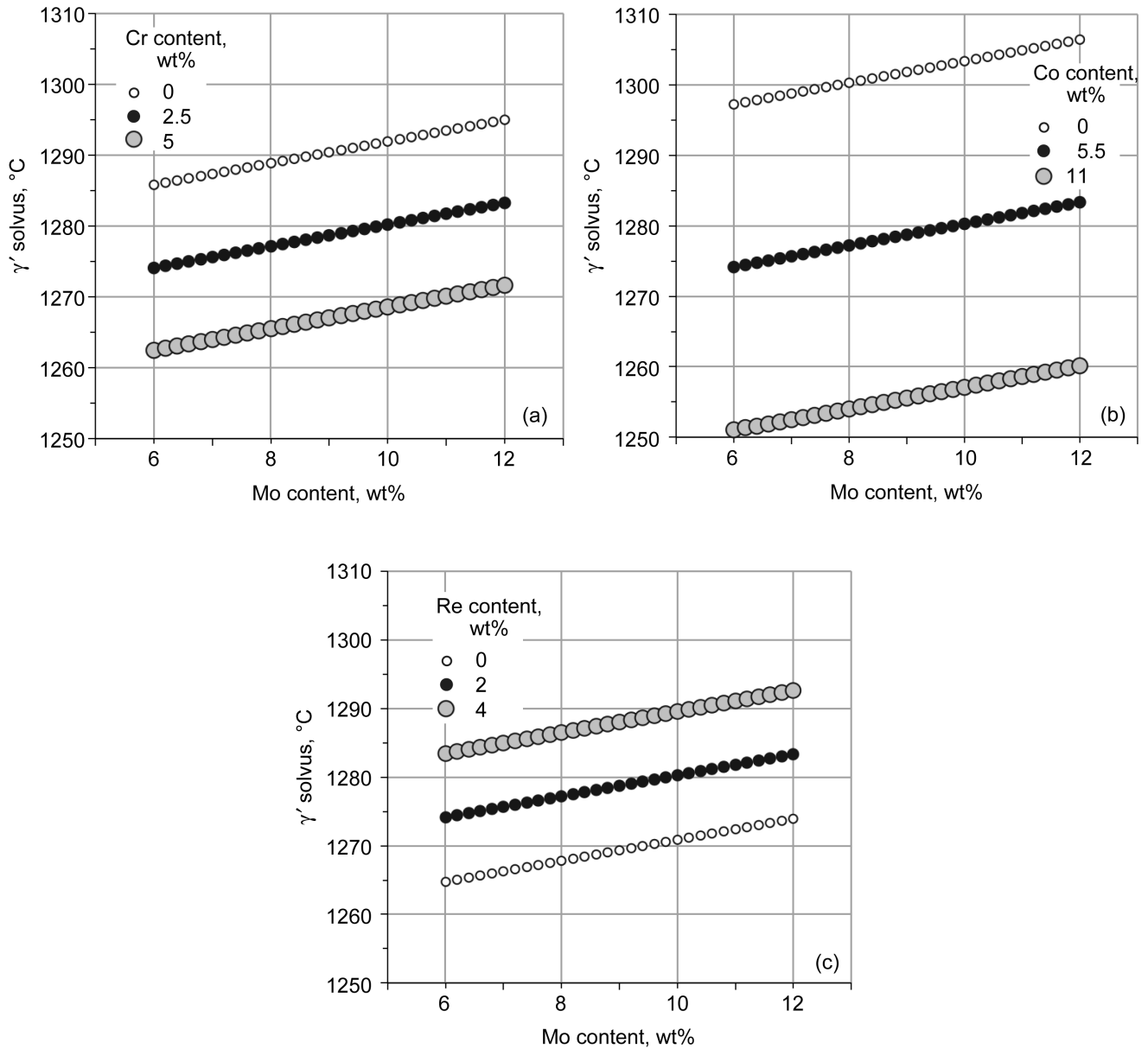
Figure 2.—Regression model output curves for estimated γ′ solvus as a function of bulk Mo content. (a) 0, 2.5, and 5.0 wt% Cr, with Co and Re fixed at their midrange levels (5.5 and 2 wt%, respectively). (b) 0, 5.5, and 11 wt% Co, with Cr and Re fixed at their midrange levels. (c) 0, 2, and 4 wt% Re, with Cr and Co fixed at their midrange levels.

TABLE II.—γ′ SOLVUS AND γ′ VOLUME FRACTION

| Alloy	γ′ solvus, °C			γ′ volume fraction at 982 °C, vol%			γ′ volume fraction at 1093 °C, vol%		
	Measured	Estimated by regression model	Predicted by JMatPro	Measured	Estimated by regression model	Predicted by JMatPro	Measured	Estimated by regression model	Predicted by JMatPro
LDS–0010	1309.0	1308.8	1303.0	67.5	67.4	60.5	58.8	59.0	48.3
LDS–0101	1273.3	1273.7	1264.9	61.5	61.7	47.9	52.2	52.6	35.4
LDS–5051	1306.1	1307.1	1289.9	65.2	65.4	60.4	55.1	54.8	47.0
LDS–5555	1282.0	1279.8	1270.5	64.1	63.8	55.8	54.5	53.3	42.3
LDS–4583	1278.6	1277.5	1263.0	62.5	62.8	57.3	50.8	50.9	43.0
LDS–4183	1255.8	1256.8	1246.6	61.6	61.9	55.8	48.7	49.2	40.0
LDS–4164	1253.3	1254.0	1245.6	60.4	60.1	51.2	47.0	47.6	36.7
LDS–1000	1278.7	1278.8	1276.3	60.1	60.1	55.9	50.6	51.1	42.6
LDS–1501	1270.2	1271.6	1257.6	61.2	61.4	56.1	48.9	49.3	41.6
LDS–1101	1249.2	1251.6	1240.8	60.3	60.4	52.3	48.8	47.9	36.8
LDS–1164	1253.0	1253.9	1244.1	60.3	60.0	52.4	47.5	47.0	37.8
LDS–1101+Hf	1256.7	1250.9	1245.4	61.0	60.7	56.3	48.1	47.7	40.9
LDS–1182	1247.0	1247.6	1237.8	60.9	61.0	54.3	48.1	48.3	37.4
LDS–1110	1244.5	1245.8	1224.9	64.0	64.0	54.8	50.4	50.9	35.6
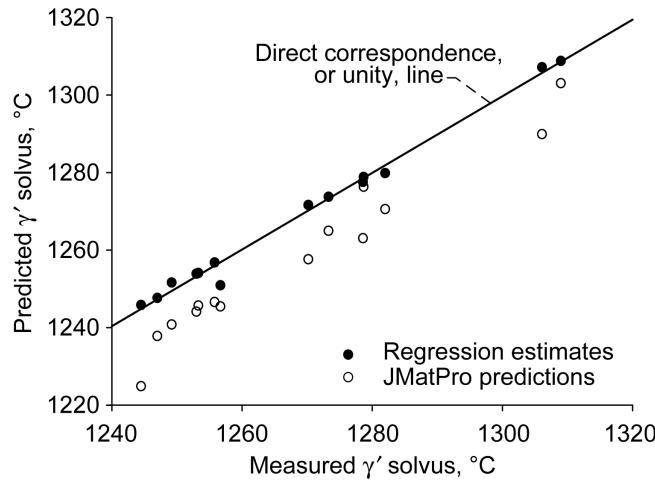
Figure 3.—Predicted versus measured γ′ solvus is shown for regression estimates determined in this study and for JMatPro 6.0 predictions.

γ′ Volume Fraction

The volume fraction of the γ′ phase was obtained from longitudinal sections of creep rupture tested specimens. During creep rupture testing, all LDS alloys developed lamellar γ-γ′ microstructures, also called γ′ rafting (Refs. 8, 9, and 22 to 25), which formed perpendicular to the applied stress direction. This γ-γ′ morphology was very amenable to quantitative assessment. However, since the creep samples were slowly furnace cooled after rupture, the γ′ volume fraction in the post-tested specimens was not representative of that at the test temperature. As a result, sections of the specimen gauge lengths were reheated, held at the testing temperature for 0.5 h, and then water quenched to freeze in the microstructure. Area fractions of the γ′ phase were then determined for each alloy at each creep testing temperature. Figures 4 and 5 display the γ-γ′ microstructures that were representative of testing at 982 and 1093 °C, respectively, for selected LDS alloys. The area fraction of γ′ can be considered equivalent to the volume fraction in this case, since the extent of γ′ through the depth can be reasonably assumed to be equal to that across the field of view used for measurement. It was
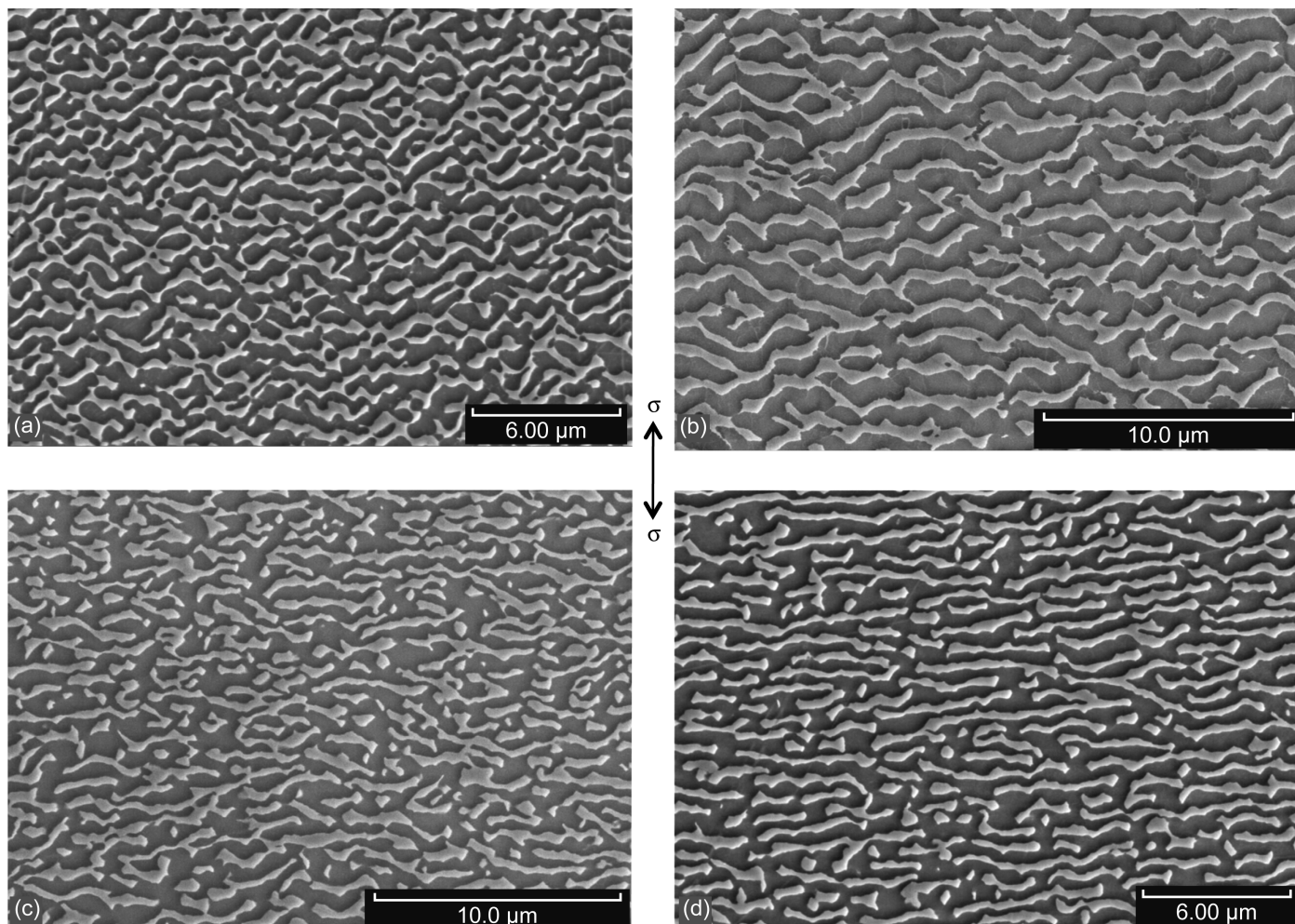
Figure 4.—γ - γ¢ microstructures representative of 982 °C creep testing. The γ¢ phase is dark, and the γ phase is bright. The applied stress (σ) direction is shown. (a) LDS–0101 at 172 MPa and 419 h. (b) LDS–1000 at 172 MPa and 273 h. (c) LDS–1101 at 241 MPa and 304 h. (d) LDS–4583 at 241 MPa and 216 h.

evident by comparing the darker phase (γ¢) in the micrographs of Figures 4 and 5 that the γ¢ volume fraction for each alloy was higher at 982 °C.

The measured volume fraction of γ¢ is shown as a function of temperature from 760 to 1310 °C for a subset of the LDS alloys in Figure 6. The alloys displayed in the figure bracket the range in γ¢ volume fractions observed at 982 and 1093 °C. Although the majority of data was obtained from specimens creep tested at 982 and 1093 °C, additional measurements were acquired from selected alloys creep tested at 760, 816, 871, and 1038 °C. The γ¢ solvus temperatures are represented at 0 vol% in Figure 6 and were obtained from the previously described DTA measurements. The alloys chosen for the figure also bracket the range in solvus temperatures observed. Figure 6 and Table II show that the volume fraction of γ¢ was above 60 vol% for all the alloys at 982 °C, but the amount of this phase decreased steadily as the temperature increased from 982 °C to the solvus temperatures.

Linear regression models were developed to estimate the effect of composition on γ¢ volume fraction at 982 and 1093 °C. The analyzed chemistries of the elements that were intentionally varied in the bulk alloys were used in the multiple linear regression analyses. The resultant regression models for each testing temperature follow:

$$\gamma\text{¢ volume fraction at 982 °C} = 63.590 - \mathbf{0.731}\ Cr\text{¢} \\ - \mathbf{1.073}\ Co\text{¢} + \mathbf{3.511}\ Mo\text{¢} + \mathbf{1.544}\ Re\text{¢}$$

with R^2_{adj} = 98.2% and rmsE = 0.296 vol%   (2)

$$\gamma\text{¢ volume fraction at 1093 °C} = 52.770 - \mathbf{2.516}\ Cr\text{¢} \\ - \mathbf{1.878}\ Co\text{¢} + \mathbf{1.796}\ Mo\text{¢}$$

with R^2_{adj} = 96.2% and rmsE = 0.662 vol%   (3)

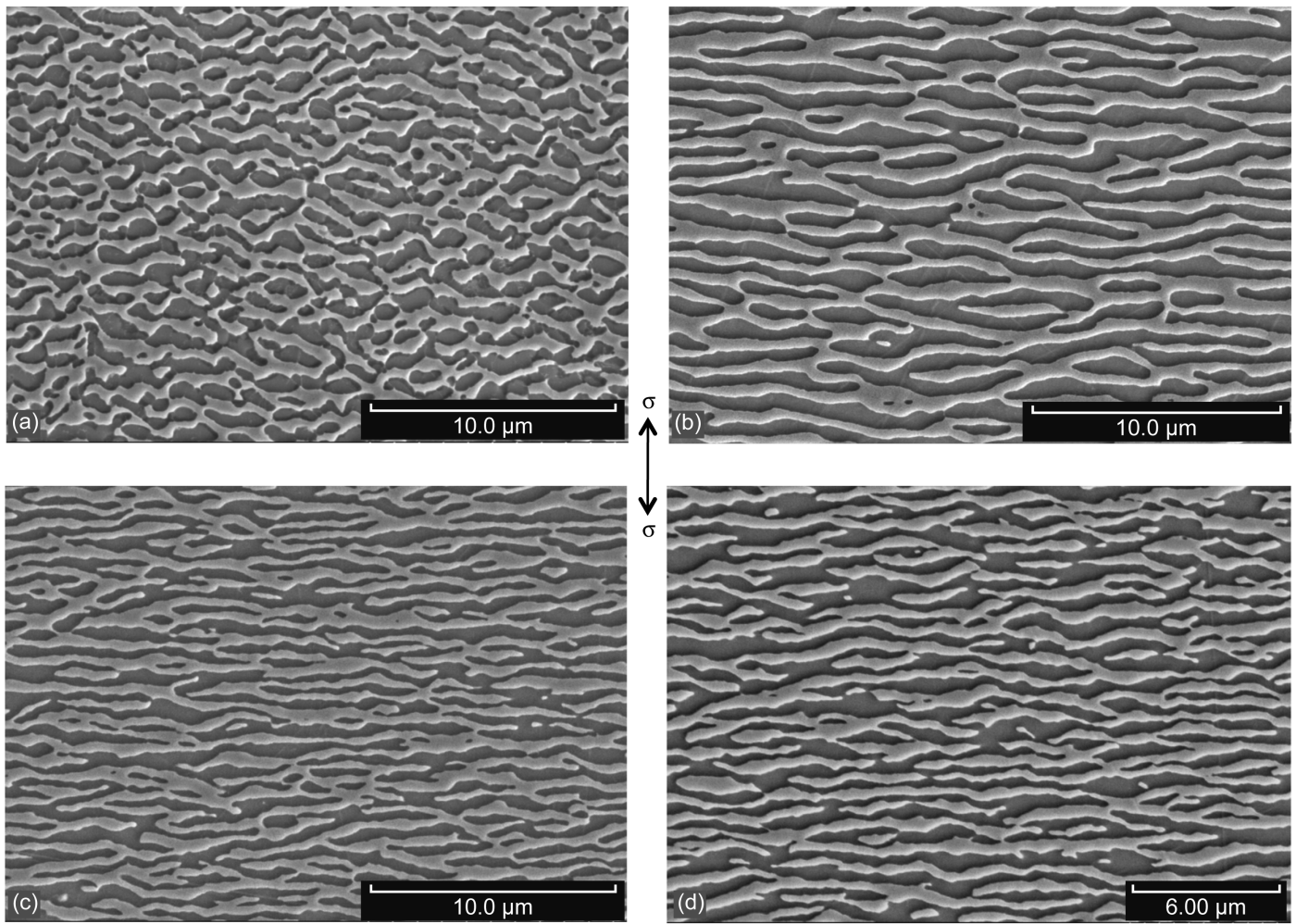where the γ¢ volume fraction is in volume percent and the terms with prime marks are the same as those defined for

Figure 5.—γ - γ¢ microstructures representative of 1093 °C creep testing. The γ¢ phase is dark, and the γ phase is bright. The applied stress (σ) direction is shown. (a) LDS–0101 at 124 MPa and 35 h. (b) LDS–1000 at 110 MPa and 150 h. (c) LDS–1101 at 124 MPa and 343 h. (d) LDS–4583 at 124 MPa and 546 h.
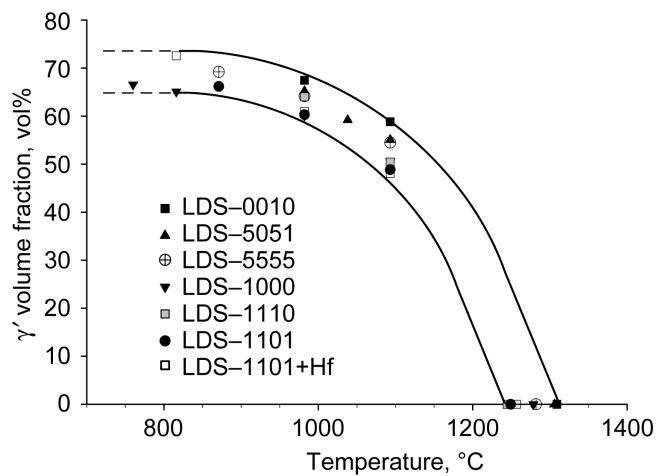

Figure 6.—Volume fraction of the γ¢ phase is displayed as a function of temperature for a subset of the low-density single crystal (LDS) alloys. The remaining LDS alloys exhibited γ¢ volume fractions within the ranges shown at 982 and 1093 °C.

Equation (1). Regression models were also developed for the γ' volume fraction using analyzed compositions in atomic percent, and no significant differences were observed with respect to either the specific terms included in the model or the goodness of fit.

The regression coefficients in Equations (2) and (3) indicate that Cr and Co decreased the γ' volume fraction at both temperatures, whereas Mo raised it. Re also increased the volume fraction at 982 °C, but it was not found to be statistically significant at 1093 °C, which is surprising since Re had an influence on γ' solvus temperatures. In addition, it

may be seen from the coefficients that Mo produced over its compositional range the biggest change in γ' volume fraction at 982 °C, whereas Cr produced the biggest change over its compositional range at 1093 °C. These influences also were evident from the model output plots in Figures 7 and 8, where the estimated changes in the value of the γ' volume fraction are displayed graphically as a function of the elements that were varied. For example, at 982 °C the steep slope of any curve in Figures 7(a) to (c) indicates that Mo raised the γ' volume fraction by 7 vol% as it was increased from 6 to 12 wt% at constant Cr, Co, and Re levels. Over their
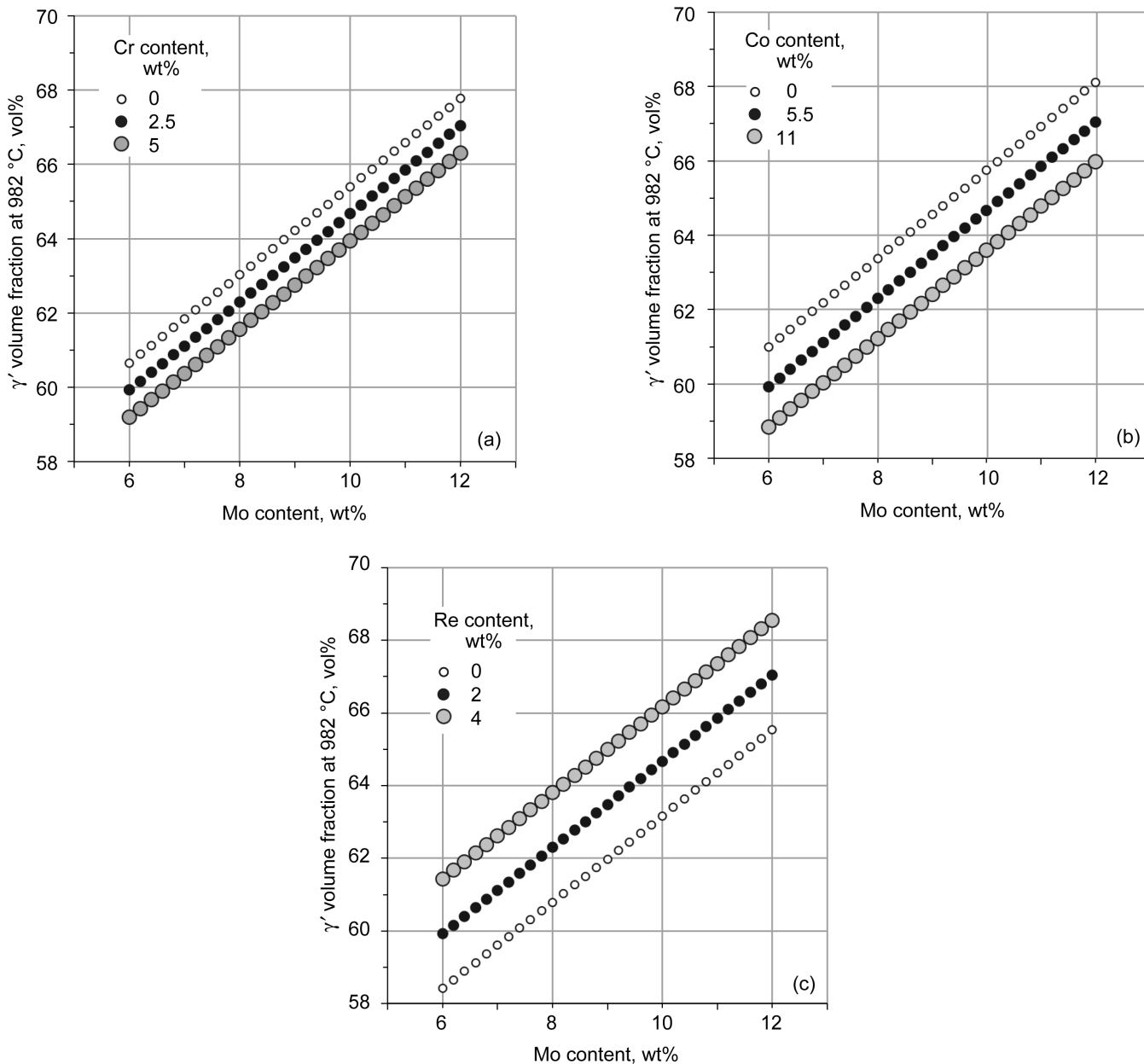

Figure 7.—Regression model output curves for estimated γ' volume fraction at 982 °C as a function of bulk Mo content. (a) 0, 2.5, and 5.0 wt% Cr, with Co and Re fixed at their midrange levels (5.5 and 2 wt%, respectively). (b) 0, 5.5, and 11 wt% Co, with Cr and Re fixed at their midrange levels. (c) 0, 2, and 4 wt% Re, with Cr and Co fixed at their midrange levels.
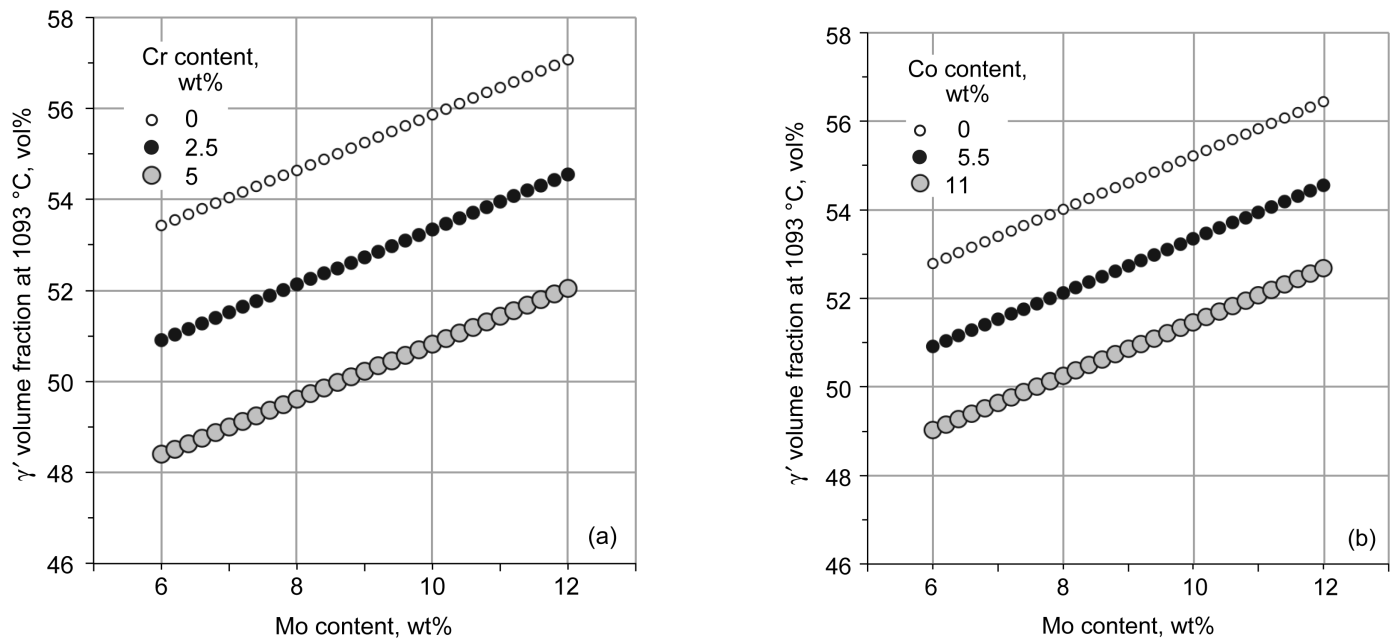
Figure 8.—Regression model output curves for estimated gȼ volume fraction at 1093 °C as a function of bulk Mo content. (a) 0, 2.5, and 5.0 wt% Cr, with Co and Re fixed at their midrange levels (5.5 wt% and 2 wt%, respectively). (b) 0, 5.5, and 11 wt% Co, with Cr and Re fixed at their midrange levels.
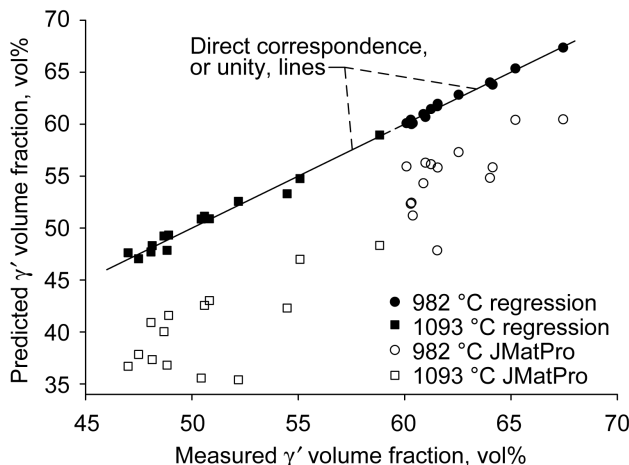

Figure 9.—Predicted versus measured gȼ volume fractions are shown at 982 and 1093 °C. The solid symbols in the figure show the excellent fit obtained by the regression models developed in this study. The open symbols demonstrate that the JMatPro predictions consistently underpredicted the measured gȼ volume fractions.

compositional ranges, Cr, Co, and Re had comparatively smaller effects on gȼ volume fraction at 982 °C, which is evident by the amount of displacement between the parallel curves in Figures 7(a), (b), and (c), respectively. Comparison of Figure 7(a) with Figure 8(a) shows that Cr had the smallest impact at 982 °C of all the compositional variables, whereas Cr had the largest impact over its compositional range on the gȼ volume fraction at 1093 °C. Figure 8(a) shows that increasing Cr from 0 to 5 wt% decreased the gȼ content at 1093 °C by 5 vol% as Mo, Co, and Re were held constant.

Figure 8(b) shows that increasing Co from 0 to 11 wt% decreased the gȼ volume fraction by 3.8 vol% and that raising Mo from 6 to 12 wt% increased the gȼ volume fraction by nearly the same amount. Thus, the effects of Cr and Co on gȼ volume fraction were larger at 1093 °C than at 982 °C, whereas the effects of Mo and Re were reduced at 1093 °C.

Figure 9 shows the excellent agreement between the measured gȼ volume fraction and that estimated by the regression models of Equations (2) and (3); the solid symbols in the figure represent these data at 982 and 1093 °C.

In contrast, JMatPro consistently underpredicted the measured γ¢ content by 7 vol% at 982 °C and by 10 vol% at 1093 °C, which is indicated by Table II and the open symbols in Figure 9. Furthermore, the JMatPro predictions exhibit a high degree of scatter, which indicates that the computational modeling tool was less accurate in predicting absolute values as well as alloy trends.

Carbides and Topologically Close-Packed Phases

The microstructure of each LDS alloy was examined in the as-solutioned condition by scanning electron microscopy. Alloys with the higher Mo contents (between 9 and 12 wt%) and no Hf addition (such as LDS–5051, LDS–5555, LDS–0010, and LDS–1110) contained blocky Mo and Ni-rich carbides in the residual interdendritic areas. X-ray diffraction on extracted carbide residue from as-solutioned bulk material indicated that these carbides were M_6C, and JMatPro predictions were in agreement with these carbide identifications. The volume fraction of carbides in these alloys was obtained by taking BSE images of five different areas at ´100 and then measuring the area fraction of the carbides using quantitative image analysis. Area fraction was considered to be a good estimate of the volume fraction because the distribution of third phases in the material was similar through the depth of material. These higher Mo content alloys typically contained about 0.5±0.1 vol% carbide in the as-solutioned condition, except for LDS–1110, which contained about 1.3±0.5 vol% carbide.

Alloys that had lower bulk Mo contents at 6 to 8 wt%, with or without Hf additions, typically contained only very minor amounts of carbides (<0.05 vol%) in the as-solutioned condition, despite the C addition that was made to each alloy. X-ray diffraction identified the carbides in the extracted residue as MC, which was in agreement with JMatPro predictions. Aging for short times of 5 h at 982 or 1093 °C tended to produce some M_6C as well, although the total volume percent of carbides remained low. It is possible that very minor amounts of M_6C were also present in these alloys in the as-solutioned condition, but such small quantities were below the detection limits.

To determine the amount of TCP phase that precipitated in these alloys, specimen gauge sections were examined after creep rupture testing for durations of up to 800 h at 982 and 1093 °C. Typical amounts and morphologies of TCP phases are shown for representative alloys without and with Hf additions in Figures 10(a) and (b), respectively. LDS–1101 is shown in Figure 10(a) after 304 h of creep testing at 982 °C; TCP laths formed in small quantities along {111} planes in the residual dendrite cores. Several creep rupture specimens of each alloy were examined at each temperature for TCP phase content. It was found that the mean volume fraction of the third phases did not change significantly after about 200 h of creep exposure, which is consistent with a previously reported study on a non-Re-bearing alloy (Ref. 26). The specific level of applied stress during creep testing also appeared to make little difference in the amount of TCP phase measured. Table III presents the average volume fraction of third phase after creep testing and subtracting off any measured amount of carbide observed in the as-solutioned state. As seen in Table III, the volume fraction of third phase was £1 vol% for most LDS alloys in this study after creep testing at either 982 or 1093 °C. Alloys with £1 vol% third phase content are considered to be stable alloys.
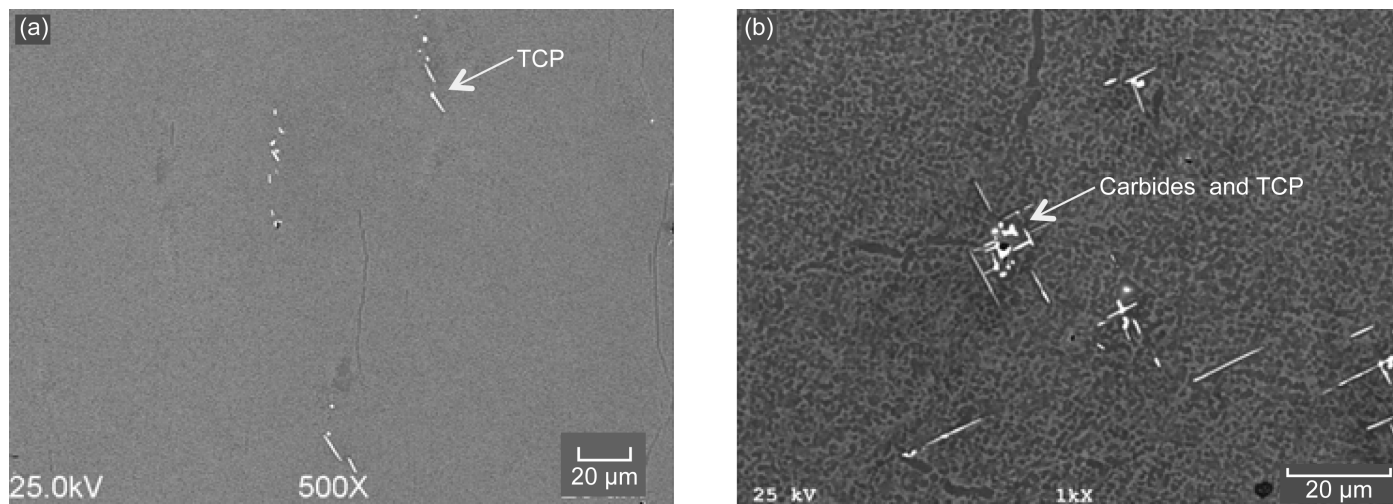

Figure 10.—Topologically closed-packed (TCP) phases and carbides observed in representative alloys. Samples were unetched and imaged using back-scattered scanning electron microscopy (BSE). (a) Without Hf addition (LDS–1101) after creep testing for 304 h at 982 °C and 241 MPa. (b) With Hf addition (LDS–4183) after creep testing for 754 h at 982 °C and 207 MPa.

TABLE III.—THIRD PHASE VOLUME FRACTIONS

Alloy	Third phase volume fraction at 982 °C, vol%		Third phase volume fraction at 1093 °C, vol%		N_{v3}	M_d	Cr + Mo + Re, wt%
	Measured	Predicted by JMatPro	Measured	Predicted by JMatPro			
LDS–0010	0	0	0	0	1.39	0.9681	12.02
LDS–0101	0	0	0	0	1.45	0.9533	9.95
LDS–5051	0.31	2.68	2.39	0.45	1.59	0.9696	14.35
LDS–5555	0.23	0.34	0.38	0	1.70	0.9708	13.38
LDS–4583	0.55	3.26	1.05	0.96	1.87	0.9763	15.02
LDS–4183	0.67	5.43	0.69	0.65	2.04	0.9814	15.11
LDS–4164	0.10	3.38	0.19	0.56	1.96	0.9717	14.12
LDS–1000	0	0	0.21	0	1.58	0.9595	11.87
LDS–1501	0.55	3.12	0.77	0.93	1.92	0.9754	15.12
LDS–1101	0.15	3.68	0.53	0	2.00	0.9745	14.72
LDS–1164	0.26	3.87	0.33	1.15	2.03	0.9754	15.00
LDS–1101+Hf	0.53	5.29	1.20	1.01	2.13	0.9832	15.33
LDS–1182	1.03	4.81	0.57	0	2.09	0.9817	15.09
LDS–1110	9.09	5.33	5.55	0	2.19	0.9920	16.63

During creep tests, LDS alloys with Hf additions typically precipitated third phases with morphologies that differed from the description provided earlier in this section because they tended to form in a cluster as a blocky phase surrounded by numerous smaller precipitates and laths, Figure 10(b). Their appearance showed evidence of the dissociation of MC into M_6C with a surrounding g¢envelope, which is consistent with the x-ray diffraction performed on extracted carbide residue. Since the amount of fine scale carbides and TCP phases was small, generally <1 vol%, no effort was made to distinguish between the two phases by BSE imaging. Thus, the volume fraction measurement obtained likely included both types of phases. Henceforth, the volume fraction measurement of TCP phases with or without carbides is referred to as third phase volume fraction for simplicity.

Two alloys (LDS–5051 and LDS–1110) were intentionally designed with higher refractory levels to precipitate higher quantities of TCP phase, and these alloys clearly did exhibit more third phase, as seen in Table III. LDS–1110 precipitated 9.1 and 5.6 vol% third phase at 982 and 1093 °C, respectively, and LDS–5051 precipitated 2.4 vol% third phase at 1093 °C. At 982 °C, LDS–5051 precipitated only 0.31 vol% third phase. EDS was performed on third phase precipitates in bulk samples as well as on third phase residue extracted from bulk samples after aging Re-bearing alloys at 982 and 1093 °C. These analyses indicated that the TCP laths contained high levels of Mo, Ni, and Re and a low level of Cr, which is consistent with observations that Re substitutes for Cr in the sigma phase of Re-containing alloys (Ref. 27). X-ray diffraction of extracted residue in the present study determined that sigma phase

precipitated in the Re-bearing alloy LDS–5051 and that mu phase precipitated in the Re-free alloy LDS–1110.

Development of linear regression models was attempted for the third phase volume fractions as a function of composition. However, because 12 of the 14 alloys had third phase quantities clustered at £1 vol%, the data set was not amenable to regression modeling. Simply put, the majority of the alloys were too stable to develop an adequate regression model.

Some serious discrepancies were found between JMatPro predictions and the measured amounts of third phase precipitation in the LDS alloys, as seen in Figure 11 and Table III. Specifically, JMatPro grossly overpredicted the amount of third phase in 9 of 14 alloys at 982 °C, which is indicated by the filled symbols in Figure 11. In addition, JMatPro significantly underpredicted by nearly 4 vol% the amount of third phase observed at 982 °C in the unstable alloy LDS–1110. However at 1093 °C, JMatPro predicted all the alloys in the design space to be essentially stable at £1.15 vol% third phase, including the two unstable alloys (LDS–1110 and LDS–5051), as shown by the open symbols in Figure 11.

Other approaches have been developed to predict TCP phase formation in complex superalloys. These include the PHACOMP method (Ref. 28), which calculates a critical electron vacancy value, N_{v3}, for the g phase in a given alloy, and the newer d-electrons concept (Ref. 29), M_d, which calculates a different critical value based on an average energy level of d orbitals of alloying elements. Both of these methods predict TCP phase instability when the alloy composition causes the parameter to exceed a critical value. The N_{v3} and M_d calculations were conducted on the current LDS alloys and
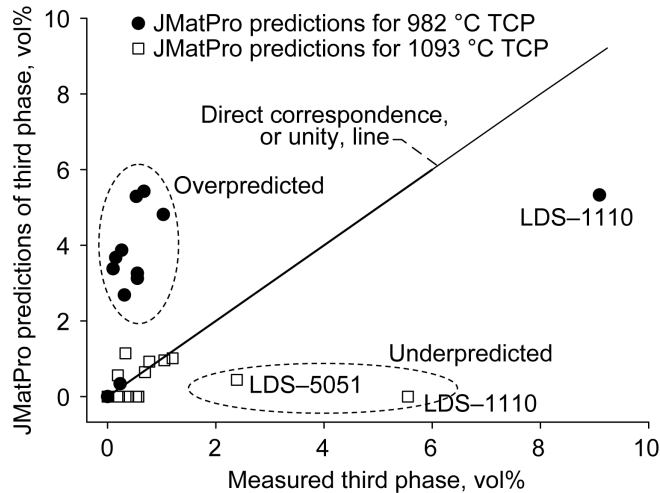
Figure 11.—Discrepancies observed between measured volume fractions of third phases and JMatPro predictions of topologically close-packed (TCP) phases at 982 and 1093 °C. JMatPro overpredicted the amount of third phase precipitation at 982 °C and underpredicted the amount of third phase in the two unstable alloys at 1093 °C.
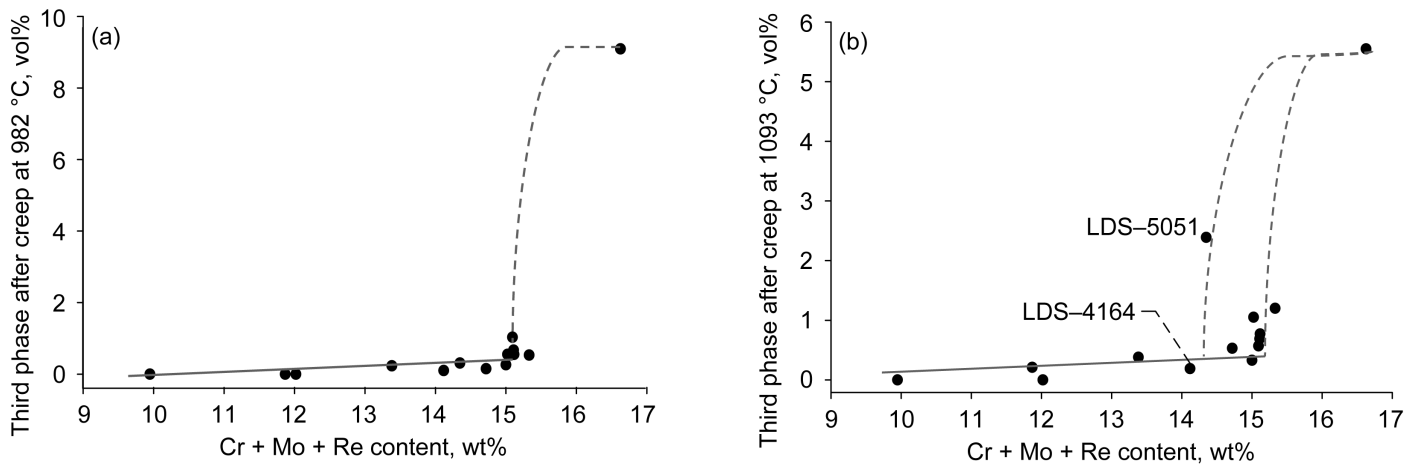

Figure 12.—Third phase volume fraction after creep testing as a function of analyzed Cr + Mo + Re levels (wt%) in the bulk. (a) At 982 °C. (b) At 1093 °C.

are listed in Table III. The interpretation of the results from these methods appears straightforward for third phase formation at 982 °C, where the single high value of third phase volume fraction occurs at $N_{v3} > 2.13$ and $M_d > 0.9832$. At 1093 °C, a transition zone exists below the critical value where approximately 1 vol% third phase can be observed in different alloys over a range of N_{v3} and M_d. Furthermore, LDS–5051 with 2.3 vol% third phase at 1093 °C was not easily explained by either of these methods because its resultant low N_{v3} and M_d values were significantly below those of stable alloys.

A very simple representation of the effects of alloying on third phase formation is shown in Figure 12. Here, the third phase volume fraction at each temperature is displayed as a function of the total refractory metal content (Cr + Mo + Re)

in the bulk alloy. The plots for each creep-testing temperature show similar features, namely that most of the alloys were stable, well below 1 vol% of third phase, but that there appeared to be a critical total refractory metal content of about 15.3 wt%, above which third phase precipitation was more noticeably induced. At 1093 °C, Figure 12(b) shows LDS–5051 to be an outlier at 14.35 wt% (Cr + Mo + Re). Closer examination of the data in the figure reveals that the alloy (LDS–4164) closest to LDS–5051 in bulk refractory metal content had a third phase volume fraction of near 0 vol% and a Co level of 11 wt%, whereas LDS–5051 exhibited 2.39 vol% third phase and had no Co addition. Co may be able to explain the difference in TCP precipitation responses between LDS–5051 and LDS–4164 since Co has been reported to improve alloy stability (Refs. 4 to 7 and 30).

It should be noted that displaying the third phase volume content as a function of total Cr + Mo + Re content in atomic percent looked somewhat similar in shape to that in Figure 12, although plots in atomic percent exhibited more scatter and did not help to explain the behavior of LDS–5051.

𝑔 and 𝑔¢ Phase Chemistries

Experimental Results

Extractions of 𝑔¢ phase were attempted on all LDS alloys in order to obtain the individual compositions of the 𝑔¢ precipitates and 𝑔 matrix after the following aging treatments in Ar: 1093 °C for 5 h plus water quenching; 982 °C for 5 h plus water quenching; and 1079 °C for 4 h and 871 °C for 12 h, followed by gas quenching to ambient temperature. The extraction results from the two-step aging treatment represented the microstructure that developed in the last aging step (i.e., 871 °C). Phase extractions were performed three times for each alloy at each temperature. Unfortunately, the Cr-free alloys and one of the midrange Cr-bearing alloys became passive during the extraction process and exhibited extremely low 𝑔¢ recoveries; no satisfactory electrolyte or electrolysis conditions were found to change this behavior. This tendency to passivate in low Cr alloys has been observed elsewhere (Ref. 31). Thus, the results described in the following paragraphs represent the trends for a subset of 10 LDS alloys having midrange to high Cr levels.

It is well known that the individual alloying elements in Ni-base superalloys exhibit distinct partitioning behavior between the 𝑔 and 𝑔¢ phases. Figure 13 displays the 𝑔/𝑔¢ partitioning ratio for each alloying element in LDS–1101 as a function of the aging
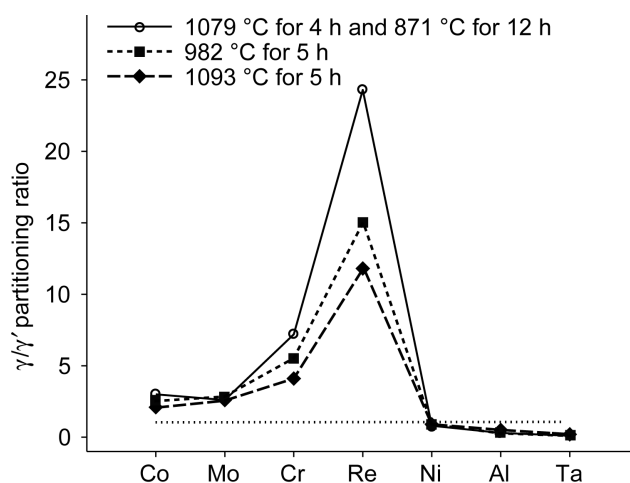
Figure 13.—𝑔/𝑔¢ partitioning ratio for each major alloying element in LDS–1101 as a function of aging temperature. The fine dotted line represents a partitioning ratio of 1.0. A partitioning ratio greater than 1.0 indicates that the element partitions to the 𝑔 matrix, and a partitioning ratio less than 1.0 indicates that the element partitions to the 𝑔¢ phase.

treatments described in the preceding paragraph. The partitioning ratio for each element is defined by the concentration of a given element in the 𝑔 matrix divided by that in the 𝑔¢ phase. A partitioning ratio greater than 1.0 indicates that the element has a higher concentration in, or partitions more to, the 𝑔 phase, whereas a partitioning ratio less than 1.0 indicates that the element partitions more to the 𝑔¢ phase. It should be noted that although bulk alloy compositions are typically described in the literature in weight percent, phase compositions are usually described in atomic percent (Refs. 4, 5, and 31 to 33). To be consistent, the phase compositions are presented in atomic percent, and the partitioning ratios are calculated from compositions in atomic percent. Figure 13 demonstrates that Cr, Co, Mo, and Re had concentrations in the 𝑔 matrix of LDS–1101 that were significantly higher than those in the 𝑔¢ phase, and thus are 𝑔 formers. In contrast, Al, Ta, Ni, and Hf had concentrations in the 𝑔¢ phase that were significantly higher than those in the 𝑔 matrix, and thus are 𝑔¢ formers. This partitioning behavior was consistent for all alloys in this study and was irrespective of the aging condition examined.

Furthermore, Figure 13 clearly shows that the partitioning ratios were not constant as a function of temperature. The 𝑔 formers had lower partitioning ratios at higher aging temperatures, and the 𝑔¢ formers exhibited the opposite trend. For examining these temperature dependencies in greater detail, it was more instructive to consider the concentrations of the individual elements in each phase independently rather than through a ratio. Thus, Table IV and Figures 14(a) to (f) show the Cr, Co, Mo, Re, Al, and Ta concentrations, respectively, in the 𝑔 phase of selected alloys as a function of temperature. Table V and Figures 15(a) to (f) display the Cr, Co, Mo, Re, Al, and Ta concentrations, respectively, in the 𝑔¢ phase of the same selected alloys as a function of temperature. These alloys represent a subset of alloys with bulk compositions containing 2.4 to 4.8 Cr, 0 to 11 Co, 6.1 to 9.5 Mo, and 0 to 4.1 Re, all in weight percent.

Figures 14(a) to (d) show that the Cr, Co, Mo, and Re concentrations in 𝑔 decreased with increasing temperature. Experimental errors were small: for example, 95% confidence intervals were typically ±0.2 at% around the mean concentrations for Cr, Co, and Mo in 𝑔 and ±0.06 at% for Re in 𝑔. In general, the 𝑔¢ formers in the 𝑔 matrix were observed to increase in concentration with increasing temperature. Figure 14(e) and Table IV show that the Al level in 𝑔 increased significantly with increasing temperature for all but one alloy, LDS–5555. The Ta concentration in 𝑔 showed very modest, but consistent, increases with increasing temperature, as seen in Figure 14(f). The 95% confidence intervals were typically ±0.2 at% around the mean concentrations for Al in 𝑔 and ±0.1 at% around the mean concentrations for Ta in 𝑔. Thus, the temperature dependence of the 𝑔 phase chemistries appeared to be related to the temperature dependence of the volume fraction of that phase. As the temperature was increased above 871 °C, the 𝑔¢ phase began to dissolve,
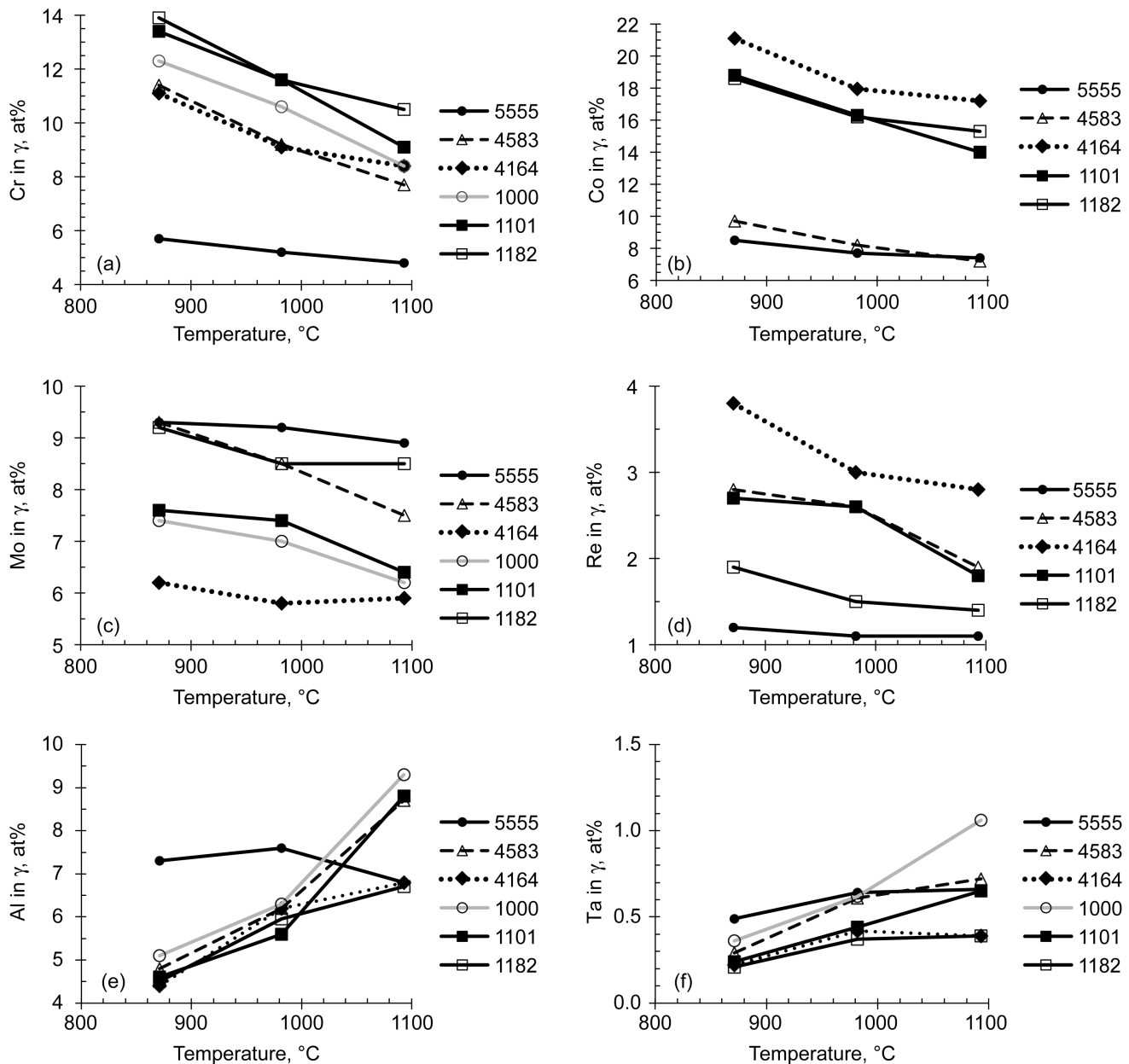
Figure 14.—Concentrations of elements in the γ matrix are shown as a function of temperature for a subset of LDS alloys. (a) Cr. (b) Co. (c) Mo. (d) Re. (e) Al. (f) Ta.

thereby releasing the γ′ formers (Hf, Ta, Al, and Ni) into the γ matrix. The lower volume fraction of γ′ equates to a higher volume fraction of γ, which dilutes the concentrations of the γ formers in the matrix and elevates the concentrations of the γ′ formers in the matrix.

In comparison, the γ′ phase chemistries varied less between alloys, and their changes as a function of temperature were also considerably smaller, as seen in Figures 15(a) to (d) and Table V. Nonetheless, the trends as a function of temperature were still remarkably consistent. The Cr and Co concentrations in γ′ were seen to increase with increasing temperature by a few tenths of an atomic percent, whereas Re in γ′

increased by a smaller fraction. Mo levels in γ′ exhibited a negative temperature dependence by consistently decreasing by 0.4 to 0.5 at% from 871 to 1093 °C. Again, the experimental errors were small since the 95% confidence intervals were ±0.06 at% for Cr, Co, and Mo in γ′ and ±0.01 at% for Re in γ′. Figure 15(e) indicates that the Al level in γ′ showed no clear trend with increasing temperature among the alloys, whereas the Ta concentration in γ′ showed modest, but consistent, increases with increasing temperature for all alloys, Figure 15(f). The 95% confidence intervals were ±0.3 at% around the mean concentrations for Al in γ and ±0.06 at% around the mean concentrations for Ta in γ.

TABLE IV.—γ COMPOSITIONS MEASURED BY PHASE EXTRACTION

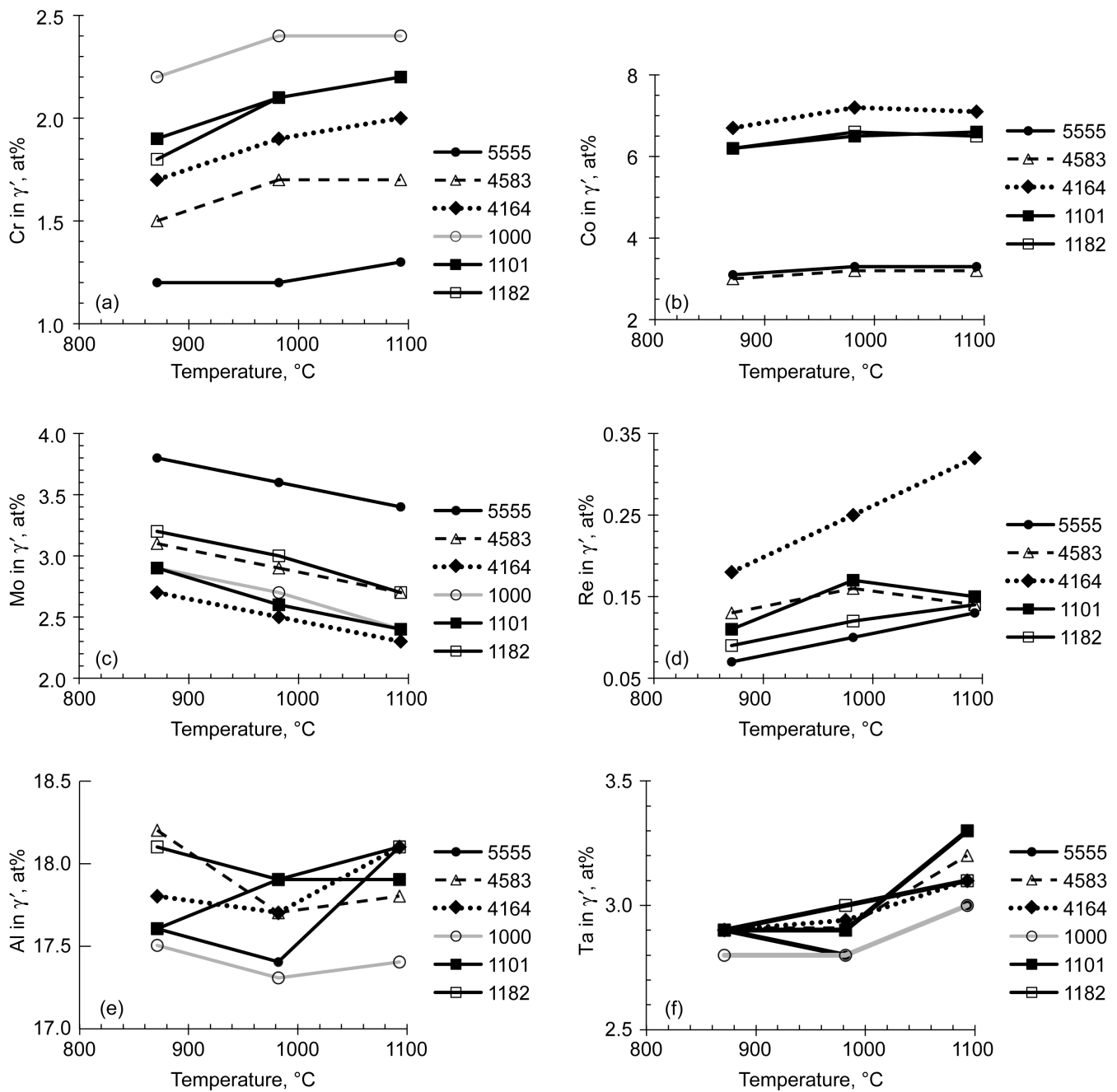| Alloy	Temperature, °C	Concentration, at%						
		Cr	Co	Mo	Re	Al	Ta	Ni
LDS–1101	871	13.4	18.8	7.6	2.7	4.6	0.24	52.6
	982	11.6	16.3	7.4	2.6	5.6	0.44	55.8
	1093	9.1	14.0	6.4	1.8	8.8	0.65	59.3
LDS–4583	871	11.4	9.7	9.3	2.8	4.8	0.29	61.6
	982	9.2	8.2	8.5	2.6	6.2	0.61	64.6
	1093	7.7	7.2	7.5	1.9	8.7	0.72	66.3
LDS–1501	871	13.8	9.8	8.0	2.7	4.5	0.26	60.8
	982	11.9	8.4	7.5	2.3	5.8	0.40	63.4
	1093	11.0	8.0	7.8	2.2	5.8	0.46	64.6
LDS–4183	871	11.5	19.0	9.2	2.9	4.5	0.22	52.7
	982	9.3	16.2	8.4	2.3	6.2	0.42	57.0
	1093	8.6	15.6	8.4	2.2	6.8	0.40	58.0
LDS–5555	871	5.7	8.5	9.3	1.2	7.3	0.49	67.4
	982	5.2	7.7	9.2	1.1	7.6	0.64	68.3
	1093	4.8	7.4	8.9	1.1	6.8	0.66	70.2
LDS–1000	871	12.3	0	7.4	0	5.1	0.36	74.8
	982	10.6	0	7.0	0	6.3	0.62	75.3
	1093	8.4	0	6.2	0	9.3	1.06	75.0
LDS–1101+Hf	871	14.5	19.0	8.2	3.0	4.6	0.21	50.5
	982	12.0	16.3	7.6	2.4	6.2	0.37	54.9
	1093	10.8	15.4	7.7	2.2	7.1	0.46	56.2
LDS–1182	871	13.9	18.6	9.2	1.9	4.5	0.21	51.6
	982	11.6	16.2	8.5	1.5	5.95	0.37	55.6
	1093	10.5	15.3	8.5	1.4	6.7	0.39	57.0
LDS–1164	871	13.8	19.2	6.4	3.7	4.4	0.20	52.2
	982	11.5	16.4	6.1	3.0	6.0	0.40	56.4
	1093	10.8	15.8	6.3	2.9	6.6	0.41	57.1
LDS–4164	871	11.1	21.1	6.2	3.8	4.4	0.22	53.1
	982	9.1	17.95	5.8	3.0	6.2	0.42	57.3
	1093	8.4	17.2	5.9	2.8	6.8	0.39	58.4

Figure 15.—Concentrations of elements in the γ′ phase are shown as a function of temperature for a subset of LDS alloys.
(a) Cr. (b) Co. (c) Mo. (d) Re. (e) Al. (f) Ta.

TABLE V.—γ′ COMPOSITIONS MEASURED BY PHASE EXTRACTION

Alloy	Temperature, °C	Concentration, at%							
		Cr	Co	Mo	Re	Al	Ta	Ni	Hf
LDS–1101	871	1.9	6.2	2.9	0.11	17.6	2.9	68.4	0
	982	2.1	6.5	2.6	0.17	17.9	2.9	67.6	0
	1093	2.2	6.6	2.4	0.15	17.9	3.3	67.4	0
LDS–4583	871	1.5	3.0	3.1	0.13	18.2	2.9	71.1	0.093
	982	1.7	3.2	2.9	0.16	17.7	2.9	71.1	0.089
	1093	1.7	3.2	2.7	0.14	17.8	3.2	71.1	0.103
LDS–1501	871	1.8	2.9	2.8	0.10	17.2	2.9	71.7	0.083
	982	2.07	3.1	2.6	0.15	17.9	3.0	70.8	0.108
	1093	2.2	3.1	2.4	0.19	18.1	3.2	70.4	0.102
LDS–4183	871	1.6	6.3	3.3	0.11	17.8	2.9	68.0	0.078
	982	1.76	6.7	3.1	0.16	17.8	2.9	67.4	0.086
	1093	1.8	6.6	2.8	0.21	18.1	3.0	67.2	0.105
LDS–5555	871	1.2	3.1	3.8	0.07	17.6	2.9	71.3	0
	982	1.2	3.3	3.6	0.10	17.4	2.8	71.1	0
	1093	1.3	3.3	3.4	0.13	18.1	3.0	70.5	0
LDS–1000	871	2.2	0	2.9	0	17.5	2.8	74.5	0
	982	2.4	0	2.7	0	17.3	2.8	74.8	0
	1093	2.4	0	2.4	0	17.4	3.0	74.8	0
LDS–1101+Hf	871	1.8	6.3	2.9	0.11	18.1	3.0	67.8	0.081
	982	2.1	6.6	2.7	0.15	18.1	3.0	67.1	0.088
	1093	2.3	6.6	2.4	0.21	18.3	3.2	66.8	0.095
LDS–1182	871	1.8	6.2	3.2	0.09	18.1	2.9	67.6	0.094
	982	2.1	6.6	3.0	0.12	17.9	3.0	67.0	0.115
	1093	2.2	6.5	2.7	0.14	18.1	3.1	67.0	0.116
LDS–1164	871	1.9	6.0	2.6	0.19	18.3	2.9	68.0	0.085
	982	2.1	6.4	2.4	0.23	18.0	3.0	67.5	0.104
	1093	2.2	6.4	2.1	0.28	18.2	3.2	67.4	0.091
LDS–4164	871	1.7	6.7	2.7	0.18	17.8	2.9	67.8	0.081
	982	1.9	7.2	2.5	0.25	17.7	2.94	68.2	0.090
	1093	2.0	7.1	2.3	0.32	18.1	3.1	66.8	0.107

Regressions of γ Phase Chemistries

Multiple regression analyses were performed on the subset of 10 LDS alloys to determine the effect of Cr, Co, Mo, and Re in the bulk alloy on the γ phase chemistries at 871, 982, and 1093 °C. The regression models generated were as follows:

Cr in $\gamma_{871\,°C}$ = 9.85 + **4.27** Cr* + **0.56** Mo* + **0.71** Re*
with R^2_{adj} = 98.8% and rmsE = 0.28 at%   (4a)

Co in $\gamma_{871\,°C}$ = 10.26 + **0.34** Cr* + **10.12** Co* + **0.51** Re*
with R^2_{adj} = 99.9% and rmsE = 0.15 at%   (4b)

Mo in $\gamma_{871\,°C}$ = 8.16 + **0.73** Cr* + **2.26** Mo*
with R^2_{adj} = 92.4% and rmsE = 0.33 at%   (4c)

Re in $\gamma_{871\,°C}$ = 1.88 + **1.91** Re*
with R^2_{adj} = 99.3% and rmsE = 0.10 at%   (4d)

Al in $\gamma_{871\,°C}$ = 5.59 – **1.06** Cr* – **0.57** Re*
with R^2_{adj} = 77.7% and rmsE = 0.41 at%   (4e)

Ta in $\gamma_{871\,°C}$ = 0.35 – **0.09** Cr* – **0.08** Co*
with R^2_{adj} = 86.8% and rmsE = 0.03 at%   (4f)

Cr in $\gamma_{982\,°C}$ = 8.50 + **3.33** Cr*
with R^2_{adj} = 98.3% and rmsE = 0.27 at%   (5a)

Co in $\gamma_{982\,°C}$ = 8.91 + **0.21** Cr* + **8.96** Co*
with R^2_{adj} = 99.9% and rmsE = 0.13 at%   (5b)

Mo in $\gamma_{982\,°C}$ = 7.76 + **0.49** Cr* + **2.04** Mo*
with R^2_{adj} = 98.2% and rmsE = 0.14 at%   (5c)

Re in $\gamma_{982\,°C}$ = 1.61 + **1.56** Re*
with R^2_{adj} = 97.1% and rmsE = 0.16 at%   (5d)

Al in $\gamma_{982\,°C}$ = 6.58 – **0.74** Cr*
with R^2_{adj} = 72.3% and rmsE = 0.26 at%   (5e)

Ta in $\gamma_{982\,°C}$ = 0.56 – **0.09** Cr* – **0.11** Co*
with R^2_{adj} = 83.1% and rmsE = 0.04 at%   (5f)

Cr in $\gamma_{1093\,°C}$ = 7.39 + **2.74** Cr* + **0.72** Re*
with R^2_{adj} = 91.6% and rmsE = 0.56 at%   (6a)

Co in $\gamma_{1093\,°C}$ = 8.41 + **8.51** Co*
with R^2_{adj} = 99.2% and rmsE = 0.49 at%   (6b)

Mo in $\gamma_{1093\,°C}$ = 7.67 + **1.55** Mo*
with R^2_{adj} = 75.3% and rmsE = 0.54 at%   (6c)

Re in $\gamma_{1093\,°C}$ = 1.41 + **1.41** Re*
with R^2_{adj} = 97.8% and rmsE = 0.13 at%   (6d)

Ta in $\gamma_{1093\,°C}$ = 0.69 – **0.30** Co*
with R^2_{adj} = 74.4% and rmsE = 0.11 at%   (6e)

Here the concentration of an element in the γ phase is given in atomic percent. In these equations, the terms followed by asterisks represent the normalized form of each significant element in the bulk composition for the subset of alloys. This form is the difference between the analyzed element content and the midpoint of the range of that element in the subset divided by the half-range of that element in the subset— all in atomic percent. Thus, Cr* = [(Cr – 4.225)/1.445], Co* = [(Co – 5.575)/5.575], Mo* = [(Mo – 4.835)/1.045], and Re* = [(Re – 0.655)/0.655].

The regression equations show that Cr, Co, Mo, and Re in the bulk not only affected the concentration of that element in the γ phase, but any given element in the bulk was often seen to affect the concentrations of other elements in the γ phase. For example, Equation 4(a) shows that bulk Cr, Mo, and Re levels all affected the Cr concentration in the γ phase at 871 °C; the regression model output curves display the magnitude of these influences very effectively. Figure 16(a) indicates that the concentration of Cr in the γ phase at 871 °C was estimated to increase very significantly from 5.6 to 14.1 at%, as Cr was increased in the bulk from 2.78 to 5.67 at%, while the bulk Mo and Re were held at their midrange levels. The figure also indicates that the Cr concentration in γ was estimated to increase from 9.3 to 10.4 at% as the bulk Mo content was increased over its full range and the bulk Cr and Re were held constant at their midrange levels. Figure 16(b) shows that the Cr concentration in γ also was estimated to increase from 9.1 to 10.6 at% at 871 °C, as the Re content in the bulk was increased over its full range, with the bulk Cr and Mo held at their midrange contents. Based on Equations (4) and (5), bulk Cr content may also be seen to have an influence on the Co, Mo, Al, and Ta concentrations in the γ phase at 871 and 982 °C. However, at 1093 °C the bulk Cr content was only seen to affect the concentration of Cr in the γ phase.

The Co concentration in γ at 871 °C was affected by the Cr, Co, and Re contents in the bulk, as seen in Equation 4(b). The bulk Co content was only observed to affect the Co and Ta concentrations in the γ phase and was not found to influence the refractory metal concentrations in γ. The regression model estimates that increasing the Co level in the bulk from 0 to 11.1 at% increased Co in the γ phase by 20.2 at% at 871 °C, with Cr and Re held at their midrange values. Comparison of Equations 4(b), 5(b), and 6(b) shows that as the aging temperature was increased, fewer bulk element variables influenced the Co concentration in the γ phase. At 1093 °C, only the Co content in the bulk affected the Co concentration in the γ phase.
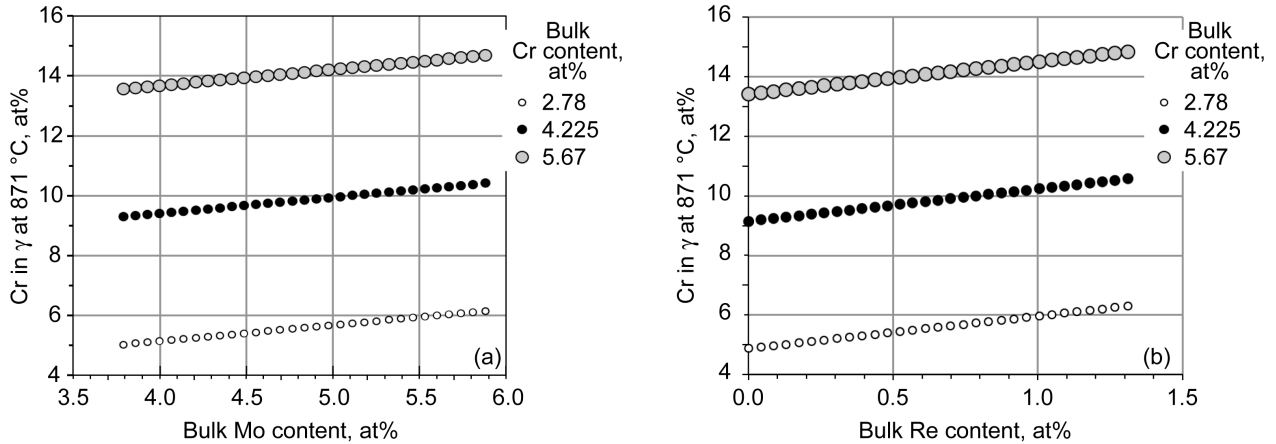
Figure 16.—Regression model output curves for the estimated Cr concentration in the γ phase at 871 °C. (a) As a function of the bulk Mo content at 2.78, 4.225, and 5.67 at% Cr with Re fixed at its midrange level. (b) As a function of the bulk Re content at 2.78, 4.225, and 5.67 at% Cr with Mo fixed at its midrange level.
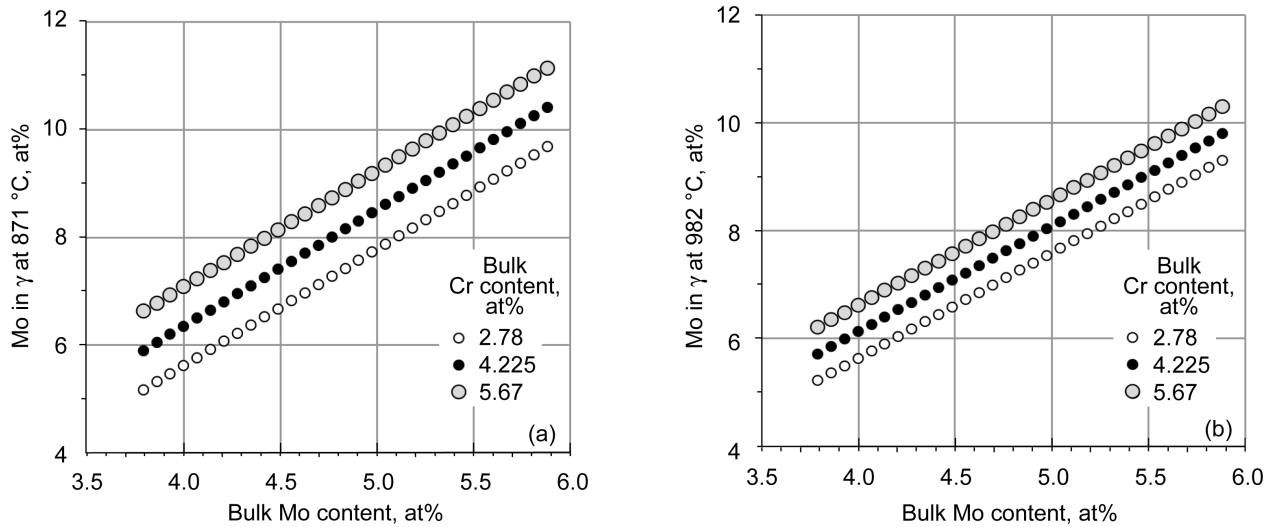

Figure 17.—Regression model output curves for the estimated Mo concentration in the γ phase as a function of the bulk Mo content at 2.78, 4.225, and 5.67 at% Cr. (a) At 871 °C. (b) At 982 °C.

The temperature dependencies of Cr and Co followed similar trends in that fewer main element terms affected their concentrations in the γ phase at 1093 °C compared to 871 °C. This result is consistent with the temperature dependence of the γ phase chemistries being related to the temperature dependence of the volume fraction of that phase. As the temperature increased, more γ′ phase went into solution and a higher volume fraction of γ phase resulted. This diluted the concentrations of the γ formers in the matrix and reduced the influence of a given γ former on the concentration of other elements in the γ phase. Overall, both Cr and Co seemed to follow this trend, where the magnitudes of the coefficients in the regression equations became smaller, and the number of significant terms in the regression equations was reduced, as the temperature increased.

At 871 °C, the Mo concentration in the γ phase was affected only by Mo and Cr in the bulk, as seen in Equation 4(c). The bulk Mo content had the most significant effect on the Mo content in γ, as indicated by the magnitude of the Mo* coefficient in the regression equation. The model output curves in Figure 17(a) demonstrate further that increasing the bulk Mo content over its full range was estimated to raise the Mo concentration in γ at 871 °C from 5.9 to 10.4 at%, with bulk Cr held at its midrange level of 4.225 at%. Figure 17(a) also indicates that increasing the bulk Cr content over its full range was estimated to raise the Mo concentration in γ from 7.4 to 8.9 at%, with bulk Mo held at its midrange level. As the temperature increased to 982 °C, the effect of bulk Cr content on the Mo concentration in γ decreased, which is shown by the comparative displacement of model output curves in Figures 17(a) and (b). With further increases in temperature to 1093 °C, the bulk Cr content had no significant effect on the Mo concentration in the γ phase, as shown by the absence of the Cr* term in Equation 6(c).

The regression equations indicate that the bulk Re content had wide-ranging effects by exerting an influence on the Cr, Co, Re, and Al concentrations in the γ phase at 871 °C, as seen in Equations 4(a), (b), (d), and (e), respectively. For example, the Cr and Co concentrations in γ were estimated to increase by 1.4 at% Cr and 1.1 at% Co, respectively, with an increase in the bulk Re content from 0 to 1.3 at% and other bulk elements held constant. However, in contrast to the other γ formers, the Re concentration in γ was only affected by the bulk Re content. This singular influence was apparent in the regression equations for all temperatures studied and likely stems from the extremely strong partitioning behavior of Re. The dilution in the concentration of the γ formers in the matrix as the γ′ phase goes into solution with increasing temperature is best exemplified in Figure 18 by the reduction in the slope of the regression model output curves for Re in γ. As shown in the figure, the Re concentration in the γ phase was estimated to decrease from 3.8 to 2.8 at% in an alloy with a bulk Re content of 1.3 at% as the temperature was increased from 871 to 1093 °C.

Multiple linear regression analyses showed that even the concentrations of the strong γ′ formers in the γ matrix were influenced by the bulk alloying elements. For example, the Al concentration in the γ phase was influenced by bulk Cr and Re contents at 871 °C (Eq. (4e)) and by bulk Cr content at 982 °C (Eq. (5e)). At 1093 °C, the regression equation for Al in γ was absent because no significant terms were found for the bulk alloying elements that were varied. The Ta concentration in the γ phase was influenced by bulk Cr and Co contents at 871 and 982 °C (Eqs. (4f) and (5f)) and by bulk Co alone at
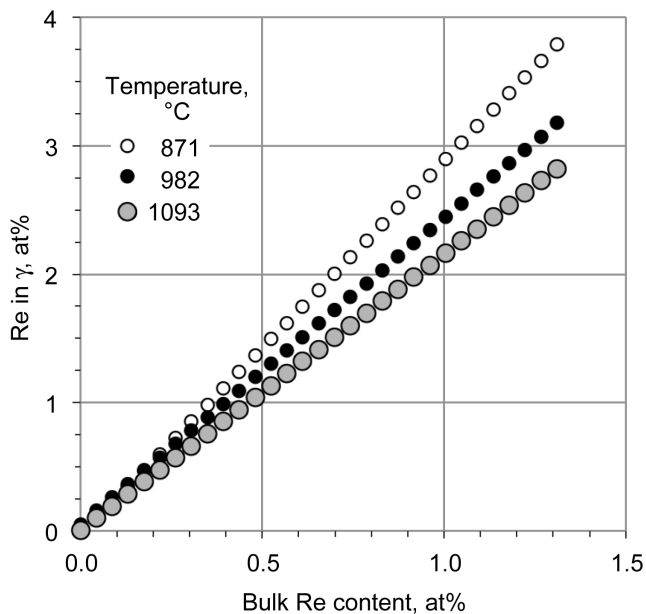
1093 °C (Eq. (6f)). Thus, the concentrations of all elements in the γ phase were influenced by fewer elements in the bulk alloy as the temperature increased and the γ phase increased in volume fraction.

Regressions of γ′ Phase Chemistries

Multiple regression analyses also were performed on the subset of 10 LDS alloys to determine the effect of Cr, Co, Mo, and Re in the bulk alloy on the γ′ phase chemistries at 871, 982, and 1093 °C. The regression models generated were as follows:

$$\text{Cr in } \gamma'_{871\,°C} = 1.64 + \mathbf{0.23}\,\text{Cr*} - \mathbf{0.26}\,\text{Mo*} - \mathbf{0.23}\,\text{Re*}$$
$$\text{with } R^2_{adj} = 96.1\% \text{ and rmsE} = 0.05 \text{ at\%} \qquad (7a)$$

$$\text{Co in } \gamma'_{871\,°C} = 3.40 + \mathbf{3.61}\,\text{Co*} - \mathbf{0.25}\,\text{Re*}$$
$$\text{with } R^2_{adj} = 99.8\% \text{ and rmsE} = 0.09 \text{ at\%} \qquad (7b)$$

$$\text{Mo in } \gamma'_{871\,°C} = 3.18 - \mathbf{0.14}\,\text{Cr*} + \mathbf{0.45}\,\text{Mo*}$$
$$\text{with } R^2_{adj} = 96.1\% \text{ and rmsE} = 0.07 \text{ at\%} \qquad (7c)$$

$$\text{Re in } \gamma'_{871\,°C} = 0.08 + \mathbf{0.09}\,\text{Re*}$$
$$\text{with } R^2_{adj} = 84.1\% \text{ and rmsE} = 0.02 \text{ at\%} \qquad (7d)$$

$$\text{Cr in } \gamma'_{982\,°C} = 1.76 + \mathbf{0.39}\,\text{Cr*} - \mathbf{0.20}\,\text{Mo*} - \mathbf{0.21}\,\text{Re*}$$
$$\text{with } R^2_{adj} = 98.6\% \text{ and rmsE} = 0.04 \text{ at\%} \qquad (8a)$$

$$\text{Co in } \gamma'_{982\,°C} = 3.61 + \mathbf{3.79}\,\text{Co*} - \mathbf{0.21}\,\text{Re*}$$
$$\text{with } R^2_{adj} = 99.9\% \text{ and rmsE} = 0.07 \text{ at\%} \qquad (8b)$$

$$\text{Mo in } \gamma'_{982\,°C} = 2.97 - \mathbf{0.16}\,\text{Cr*} + \mathbf{0.45}\,\text{Mo*}$$
$$\text{with } R^2_{adj} = 96.6\% \text{ and rmsE} = 0.07 \text{ at\%} \qquad (8c)$$

$$\text{Re in } \gamma'_{982\,°C} = 0.11 + \mathbf{0.11}\,\text{Re*}$$
$$\text{with } R^2_{adj} = 94.9\% \text{ and rmsE} = 0.02 \text{ at\%} \qquad (8d)$$

$$\text{Al in } \gamma'_{982\,°C} = 17.54 + \mathbf{0.33}\,\text{Cr*} + \mathbf{0.21}\,\text{Mo*} + \mathbf{0.35}\,\text{Re*}$$
$$\text{with } R^2_{adj} = 91.3\% \text{ and rmsE} = 0.07 \text{ at\%} \qquad (8e)$$

$$\text{Ta in } \gamma'_{982\,°C} = 2.86 + \mathbf{0.07}\,\text{Cr*} + \mathbf{0.09}\,\text{Re*}$$
$$\text{with } R^2_{adj} = 79.4\% \text{ and rmsE} = 0.04 \text{ at\%} \qquad (8f)$$

$$\text{Cr in } \gamma'_{1093\,°C} = 1.83 + \mathbf{0.39}\,\text{Cr*} + \mathbf{0.10}\,\text{Co*}$$
$$- \mathbf{0.22}\,\text{Mo*} - \mathbf{0.26}\,\text{Re*}$$
$$\text{with } R^2_{adj} = 98.1\% \text{ and rmsE} = 0.05 \text{ at\%} \qquad (9a)$$

$$\text{Co in } \gamma'_{1093\,°C} = 3.60 + \mathbf{3.76}\,\text{Co*} - \mathbf{0.20}\,\text{Re*}$$
$$\text{with } R^2_{adj} = 99.9\% \text{ and rmsE} = 0.09 \text{ at\%} \qquad (9b)$$

$$\text{Mo in } \gamma'_{1093\,°C} = 2.75 - \mathbf{0.20}\,\text{Cr*} + \mathbf{0.43}\,\text{Mo*}$$
$$\text{with } R^2_{adj} = 98.5\% \text{ and rmsE} = 0.04 \text{ at\%} \qquad (9c)$$

$$\text{Re in } \gamma'_{1093\,°C} = 0.13 + \mathbf{0.14}\,\text{Re*}$$
$$\text{with } R^2_{adj} = 84.5\% \text{ and rmsE} = 0.04 \text{ at\%} \qquad (9d)$$

Figure 18.—Regression model output curves for the estimated Re content in the γ phase as a function of the bulk Re content at 871, 982, and 1093 °C.

The concentration of an element in the g¢ phase is given in atomic percent. The terms in these equations that are followed by asterisks are defined in the same way as described for Equations (4) to (6).

Similar to that for the g phase, the regression equations show that Cr, Co, Mo, and Re in the bulk not only affected the concentration of that particular element in the g¢ phase, but a given element in the bulk was often seen to affect the concentrations of other elements in the g¢ phase. For example, at 871 °C, as Cr was increased in the bulk over its full compositional range, the Cr concentration in g¢ was estimated to increase from 1.4 to 1.9 at% (Fig. 19(a)) with bulk Mo and

Re at their midrange contents, and the Mo concentration in g¢ was estimated to decrease from 3.3 to 3.0 at% (Fig. 19(b)). These same figures also show that, at 871 °C, as bulk Mo was increased over its full range and bulk Cr was held constant at 4.225 at%, the concentration of Cr was estimated to decrease in g¢ from 1.9 to 1.4 at% (Fig. 19(a)), and the concentration of Mo in g¢ was estimated to increase from 2.7 to 3.6 at% (Fig. 19(b)). This is in agreement with early studies (Ref. 11) in which it was concluded that Mo substitutes chemically for Cr in g¢ and that Mo lowers the Cr content of g¢ in Ni-Al-Cr-Mo alloys.
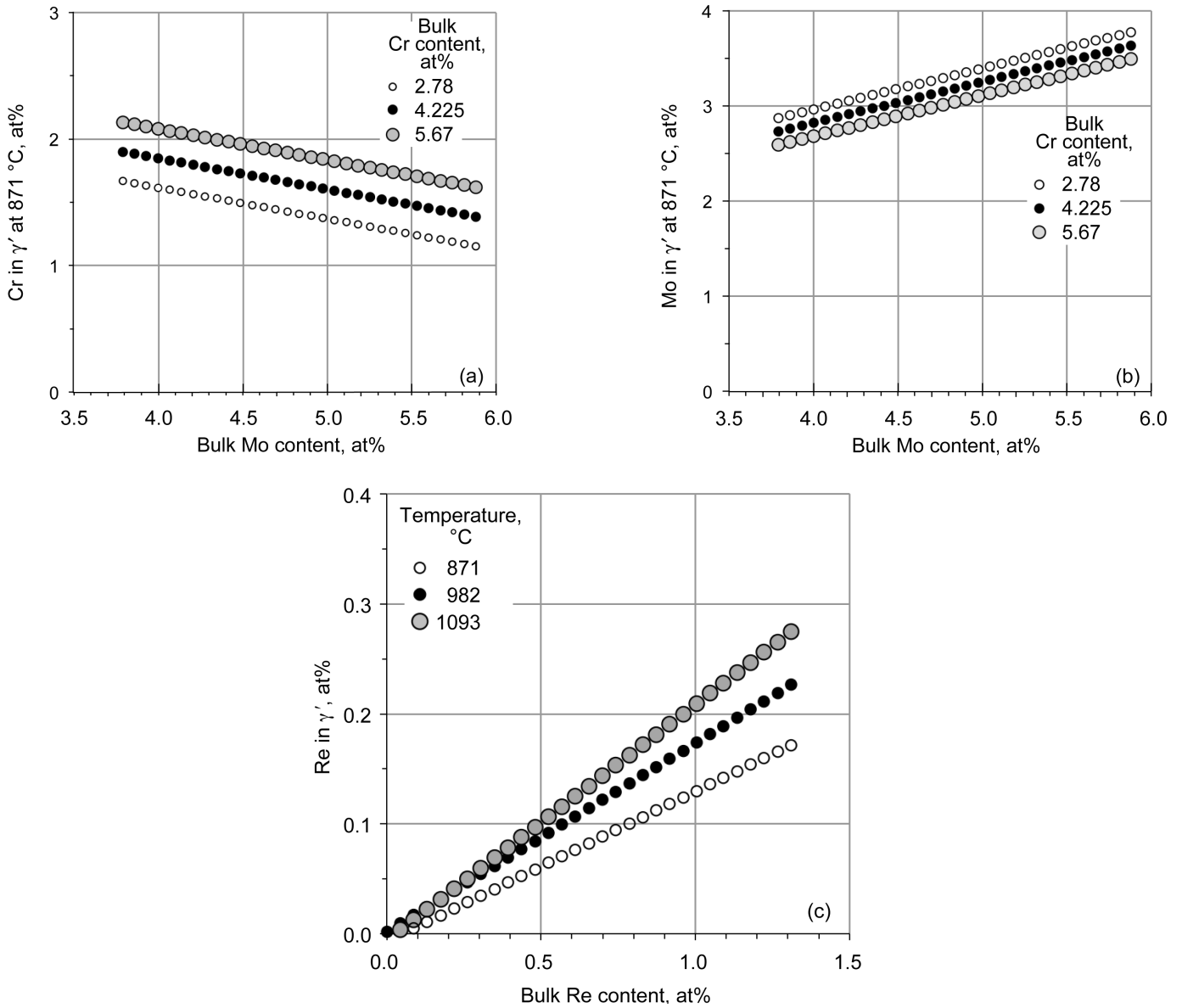

Figure 19.—Regression model output curves for the estimated g¢ phase chemistry. (a) Cr concentration in the g¢ phase at 871 °C as a function of bulk Mo content and 2.78, 4.225, and 5.67 at% Cr, with Re fixed at its midrange level. (b) Mo concentration in the g¢ phase at 871 °C as a function of the bulk Mo content and 2.78, 4.225, and 5.67 at% Cr. (c) Re concentration in the g¢ phase as a function of bulk Re content at 871, 982, and 1093 °C.

Equations (7) to (9) show that bulk Co content primarily affected the Co concentration in γ', although bulk Co had a small influence on the Cr content in γ' at 1093 °C. Increasing the Co level in the bulk alloy from 0 to 11.1 at% Co was estimated to increase the concentration of Co in the γ' phase by 7.2 at% Co at 871 °C.

Regression analyses and the model output curves in Figure 19(c) indicated that increasing Re in the bulk alloy from 0 to 1.31 at% only modestly increased the Re concentration in γ' by 0.17 at% at 871 °C, which demonstrates the strong partitioning behavior of Re to the γ phase. Figure 19(c) also demonstrates that the concentration of Re in γ' slightly increased as the temperature increased and the γ' volume fraction decreased. Bulk Re content appeared to impact the Cr and Co concentrations in γ' at all temperatures studied and was estimated to decrease slightly the concentrations of Cr and Co in the γ' phase—each by 0.5 at% at 871 °C.

The influence of bulk Cr, Co, Mo, and Re contents on Al and Ta concentrations in the γ' phase was generally determined to be minimal based on regression analyses. Regression terms for bulk Cr, Mo, and Re contents on the Al and Ta concentrations in γ' were only found to be significant at 982 °C.

Lattice Parameters of γ and γ' Phases

Lattice parameters of the γ and γ' phases were measured in situ on single crystal samples at room temperature by x-ray diffraction. The alloys were solutioned and then aged in a multistep heat treatment of 1149 °C for 24 h, 1079 °C for 8 h, and 871 °C for 12 h, followed by an Ar gas quench to room temperature. This aging treatment was performed to overage the material and lose coherency between the γ and γ' phases so that unconstrained lattice parameters and unconstrained γ-γ' lattice mismatch could be obtained (Refs. 9, 34, and 35). Figures 20(a) and (b) show that the γ' precipitates in LDS–5555 and LDS–1000, respectively, had coarsened and underwent a transition to an irregular plate morphology along {001} directions after this aging treatment, which was indicative of a semicoherent γ-γ' interface (Refs. 4, 5, 8, 35, and 36). All other LDS alloys exhibited this type of microstructure, except LDS–0101. Figure 20(c) illustrates that the γ' precipitates in LDS–0101 remained mostly cuboidal and discrete, and thus the precipitates in that alloy were still primarily coherent with the γ matrix. Little, if any, TCP phase precipitation was observed in the LDS alloys after the multistep aging treatment.

X-ray diffractometer scans were obtained at ambient temperature on the LDS alloys using monochromatic Cu $K_{\alpha 1}$ radiation, and data were gathered from the $(400)_{\gamma\gamma'}$ peaks. Figure 21 displays the diffractometer scans for selected LDS alloys. Most of the alloys in this study exhibited separation between the γ and γ' peaks in the diffractometer scans, and a typical amount of peak separation is shown in Figure 21(a) for LDS–5555. Based on extensive prior work (Ref. 34), the
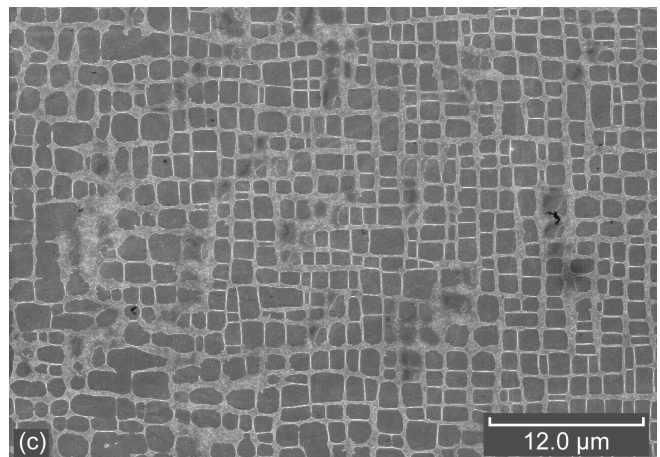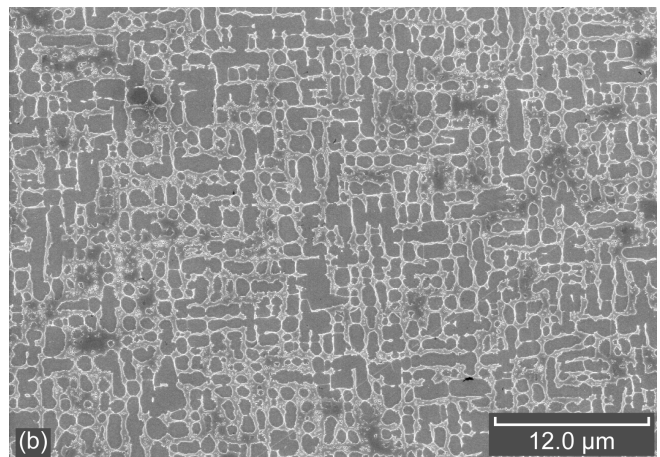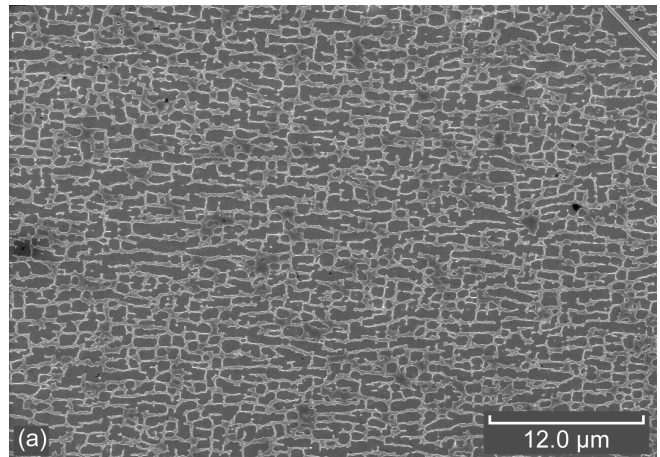

Figure 20.—γ-γ' microstructures in selected LDS alloys after a multistep aging treatment of 1149 °C for 24 h, 1079 °C for 8 h, and 871 °C for 12 h. The dark phase is γ' and the light phase is γ. (a) Interconnected γ' precipitates were evident in LDS–5555. (b) Interconnected γ' precipitates were evident in LDS–1000. (c) Precipitates were coarsened but primarily discrete in LDS–0101.
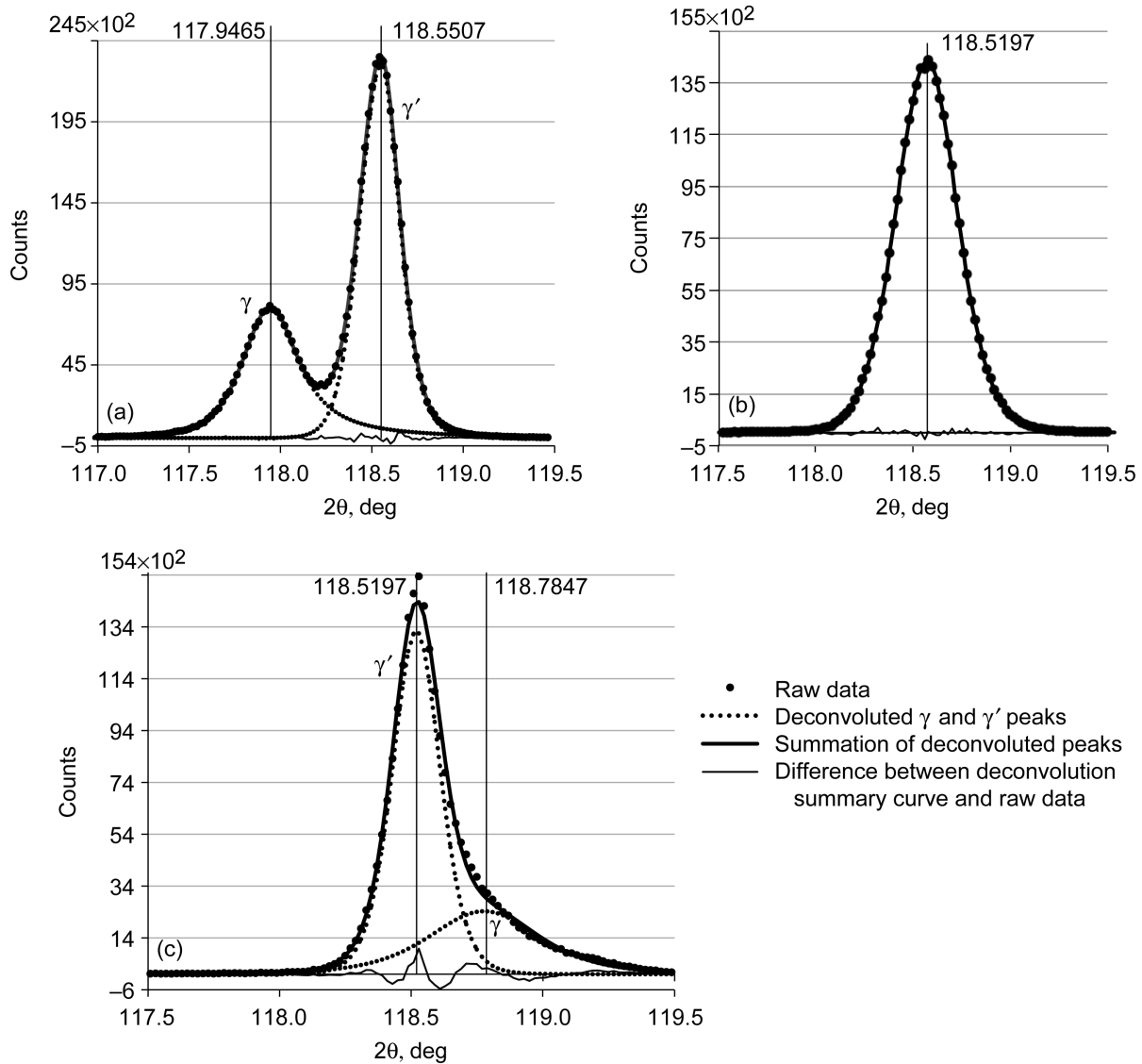
Figure 21.—X-ray diffractometer scans of {400}$_{\gamma,\gamma'}$ peaks at room temperature. (a) LDS–5555, a negative mismatch alloy. (b) LDS–1000, an alloy with near zero mismatch. (c) LDS–0101, a positive mismatch alloy.

broader peak at the lower 2θ position in Figure 21(a) represented that of the γ phase, and the narrower, higher intensity peak with higher area fraction corresponded to the γ′ phase. The fitting functions provided precise 2θ peak positions for calculating the lattice parameters of the γ and γ′ phases. As seen in Figure 21(b), LDS–1000 exhibited a single peak in which the γ and γ′ peaks could not be resolved individually since the lattice parameters of the two phases were nearly identical at room temperature. Figure 21(c) shows that the diffractometer scan for LDS–0101 exhibited a γ′ peak with a right-hand tail. The analytical fitting function was able to resolve two peaks for LDS–0101 with the broader γ peak at the higher values of 2θ. This was the only LDS alloy in the series that showed the γ peak to the right of the γ′ peak at ambient temperature.

Figure 22(a) displays the measured lattice parameters for γ and γ′ as a function of bulk Mo content in weight percent. The γ lattice parameters were typically larger than the γ′ lattice parameters, except in LDS–0101 and LDS–1000, the latter of which had indistinguishable γ and γ′ lattice parameters. The figure also shows that the γ lattice parameters generally increased as a function of Mo content, whereas the γ′ lattice parameters remained constant as a function of Mo content. These trends between the lattice parameters and the bulk Mo content were in agreement with earlier studies (Ref. 8). However, the γ lattice parameter data appeared as a widening band as the Mo content was increased, which was likely due to the influence of other alloying elements that strongly partition to the γ matrix. Thus, a linear regression model was developed for predicting the alloy composition effects on the γ lattice
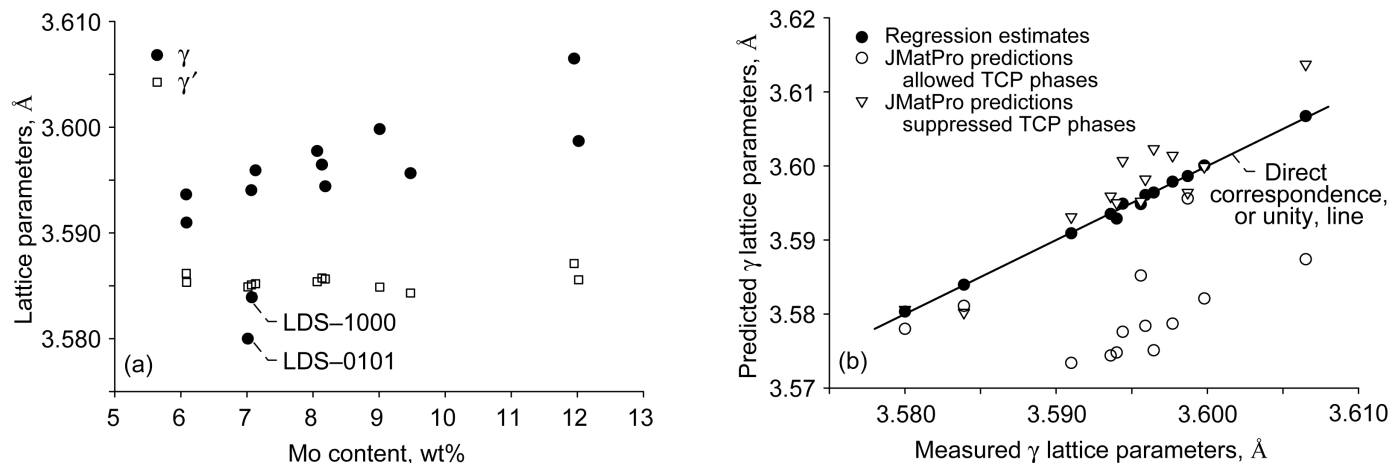
Figure 22.—Lattice parameters. (a) Room temperature lattice parameters of the γ and γ′ phases are displayed as a function of bulk Mo content. The γ′ lattice parameter is constant as a function of Mo content, but the γ lattice parameter generally increases with increasing Mo. (b) γ lattice parameters estimated by the linear regression model developed in this study are shown versus measured γ lattice parameters. JMatPro was also used to predict γ lattice parameters with two very different results.

parameter. The analyzed chemistries of the elements that were varied in the composition space were used in the multiple linear regression analyses. The following regression model was generated for the γ lattice parameter:

$$a_\gamma = 3.5949 + \mathbf{0.0065}\ Cr' - \mathbf{0.0021}\ Co' + \mathbf{0.0149}\ Mo'$$
$$+ \mathbf{0.0081}\ Re' - \mathbf{0.0013}\ Mo'Re'$$

with R^2_{adj} = 99.4%, rmsE = 0.0005 Å   (10)

where the γ lattice parameter is in angstroms, and the terms for Cr, Co, Mo, and Re that are followed by prime signs are the same as those defined for Equation (1). Mo'Re' is an interaction term of [(Mo in wt% – 9.06)/2.96] × [(Re in wt% – 2.05)/2.05]. The analysis indicated that Cr, Co, Mo, Re, and the MoRe interaction term were all significant at a probability of at least 90%.

It may be seen from the regression coefficients in Equation (10) that Cr increased the γ lattice parameter over its full range, whereas Co slightly reduced it. These compositional effects are also clearly depicted in the regression model output curves in Figures 23(a) and (b). Mo and Re also appeared to have strong effects on the γ lattice parameter, based on the magnitudes of their single variable coefficients. However, the influences of Mo and Re actually cannot be judged directly from their coefficients, because the MoRe interaction term was statistically significant and its coefficient was opposite in sign to the Mo and Re single variable terms. The compositional effects of Mo and Re on the γ lattice parameter are explained best by the regression model output curves in Figure 23(c), in which the estimated γ lattice parameters are plotted as a function of Mo for low, medium, and high levels of Re at constant Cr and Co levels. The MoRe interaction term produced nonparallel lines for 0, 2, and 4 wt% Re as a function of Mo content. From the slopes of the curves,

it may be seen that the effect of Mo on the γ lattice parameter was larger at 0 wt% Re than at 4 wt% Re. In addition, the displacement of the curves in Figure 23(c) shows that Re had a slightly greater impact at 6 wt% Mo than at 12 wt% Mo. Thus, the regression analyses clearly demonstrate that Co had the smallest effect on the γ lattice parameter and that, despite its negative interaction term, Mo had the biggest impact on the γ lattice parameter over its full compositional range.

The regression model estimates for the γ lattice parameter were in excellent agreement with the experimentally determined γ lattice parameters, as evident in Table VI and the filled symbols in Figure 22(b). Note that even the two low γ lattice parameters of LDS–0101 and LDS–1000, which did not fit the trend with Mo content in Figure 22(a), were explained well by the regression model and fit the unity line in Figure 22(b). The JMatPro predictions of the γ lattice parameters were superimposed in Figure 22(b) and are represented by the open circles in the bottom of the figure. It is clear that JMatPro grossly underpredicted the γ lattice parameters by nearly 0.02 Å, except for those in three alloys, LDS–1000, LDS–0101, and LDS–0010. These three alloys were observed experimentally to be nearly free of TCP phase (Table III) and were predicted by JMatPro to precipitate no TCP phases during high-temperature exposures. Since it was found that JMatPro frequently overpredicted the amount of TCP phase seen experimentally (Table III), it seemed quite possible that the overprediction of TCP phase could have affected the JMatPro prediction of the γ lattice parameters since the TCP phase precipitates from the γ matrix. Thus, the γ lattice parameters were subsequently redetermined in JMatPro by making selections in the software program that prevented the TCP phases from forming. By suppressing all TCP phase formation, the JMatPro predictions improved significantly for the γ lattice parameters, as indicated by Table VI and the open triangles in Figure 22(b). The γ lattice parameters were
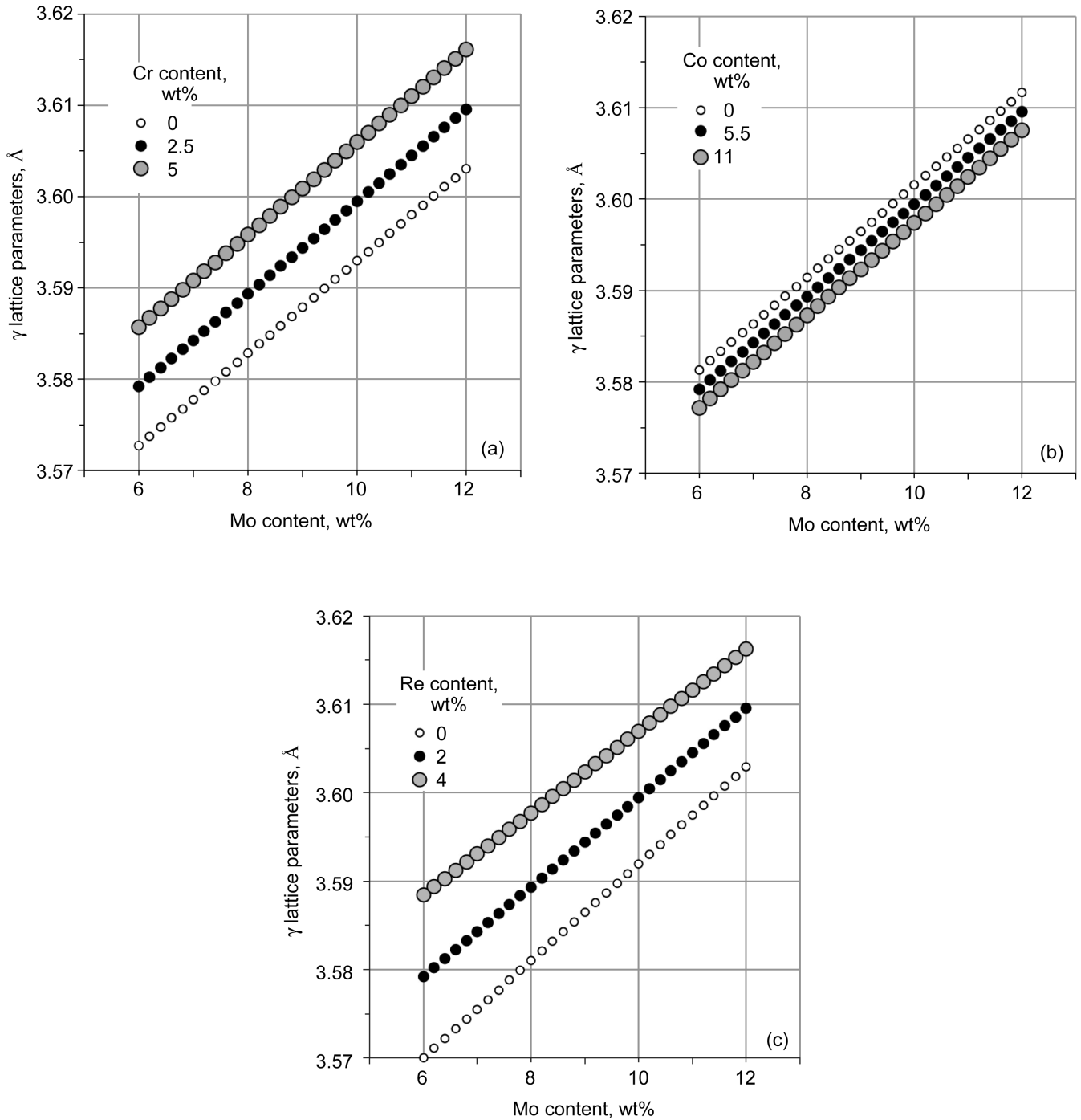
Figure 23.—Regression model output curves for estimated γ lattice parameters at room temperature as a function of bulk Mo content. (a) 0, 2.5, and 5 wt% Cr, with Co and Re fixed at their midrange levels. (b) 0, 5.5, and 11 wt% Co, with Cr and Re fixed at their midrange levels. (c) 0, 2, and 4 wt% Re, with Cr and Co fixed at their midrange levels.

TABLE VI.—LATTICE PARAMETERS AND LATTICE MISMATCH AT ROOM TEMPERATURE

Alloy	γ Lattice parameter, Å				γ′ Lattice parameter, Å			γ- γ′ Lattice mismatch, %			
	Measured	Estimated by regression model	Predicted by JMatPro		Measured	Predicted by JMatPro		Measured	Estimated by regression model	Predicted by JMatPro	
			TCP phases allowed	TCP phases sup-pressed		TCP phases allowed	TCP phases sup-pressed			TCP phases allowed	TCP phases sup-pressed
LDS–0010	3.5987	3.5986	3.5956	3.5964	3.5856	3.5867	3.5869	–0.365	–0.355	–0.245	–0.264
LDS–0101	3.5800	3.5803	3.5780	3.5806	3.5849	3.5857	3.5859	0.137	0.117	0.215	0.150
LDS–5051	3.5998	3.6001	3.5821	3.5999	3.5849	3.5834	3.5847	–0.416	–0.431	0.038	–0.422
LDS–5555	3.5956	3.5948	3.5852	3.5952	3.5843	3.5857	3.5867	–0.315	–0.278	0.013	–0.238
LDS–4583	3.5977	3.5979	3.5787	3.6014	3.5854	3.5848	3.5873	–0.344	–0.356	0.169	–0.390
LDS–4183	3.5965	3.5964	3.5751	3.6023	3.5857	3.5852	3.5884	–0.298	–0.310	0.283	–0.386
LDS–4164	3.5910	3.5909	3.5734	3.5931	3.5853	3.5844	3.5871	–0.157	–0.135	0.306	–0.167
LDS–1000	3.5839	3.5840	3.5811	3.5802	3.5839	3.5834	3.5834	0	–0.005	0.063	0.090
LDS–1501	3.5959	3.5961	3.5784	3.5982	3.5852	3.5843	3.5868	–0.298	–0.300	0.167	–0.317
LDS–1101	3.5940	3.5929	3.5748	3.5950	3.5851	3.5843	3.5869	–0.249	–0.208	0.266	–0.224
LDS–1164	3.5936	3.5935	3.5744	3.5959	3.5862	3.5842	3.5874	–0.208	–0.204	0.272	–0.237
LDS–1101+Hf	(a)	3.5951	3.5754	3.6021	(a)	3.5848	3.5885	(a)	–0.269	0.261	–0.379
LDS–1182	3.5944	3.5949	3.5776	3.6007	3.5856	3.5859	3.5890	–0.244	–0.269	0.231	–0.325
LDS–1110	3.6065	3.6067	3.5874	3.6137	3.5871	3.5866	3.5907	–0.539	–0.547	–0.023	–0.637

[a]Not measured.

slightly overpredicted in this redetermination but were moved closer to the experimentally determined values with this manipulation of the software program.

Table VI shows that the γ′ lattice parameters varied only 0.0032 Å over the entire composition space in this study, whereas the γ lattice parameters changed by nearly an order of magnitude more. A linear regression model was developed for the γ′ lattice parameter; however, the best model produced an R^2_{adj} of only 65.6%, which reflected the very small changes in lattice parameter response near the measurement resolution limit. Thus, the γ′ lattice parameter data set was strongly clustered and was not amenable to regression modeling.

JMatPro predicted the γ′ lattice parameters fairly well, as seen in Table VI, although there was some scatter in the predictions. Since the TCP phases were suppressed in the JMatPro program to improve its predictions of the γ lattice parameters, this approach was employed for consistency in determining the γ′ lattice parameter predictions. However, the predictions of JMatPro for the γ′ lattice parameters worsened with this approach, as shown in Table VI. Thus, the γ and γ′ lattice parameter predictions in JMatPro both appeared to be affected by the software's significant overprediction of the TCP phases.

γ- γ′ Lattice Mismatch

The magnitude of the elastic coherency strains between the γ and γ′ phases is determined from the unconstrained lattice mismatch δ, which is given by (Ref. 37).

$$\delta = 2\,(a_{\gamma'} - a_{\gamma})\,/\,(a_{\gamma'} + a_{\gamma}) \tag{11}$$

Equation (11) defines negative mismatch as the case in which the lattice parameter of γ is larger than that of γ′. As seen in Table VI, the majority of the LDS alloys in this study were determined experimentally to have negative values of mismatch at room temperature. A linear regression model was developed for the experimentally determined δ using the analyzed chemistries (in wt%) of the elements that were varied. The following regression model was generated:

$$\delta = -0.2820 - \textbf{0.1680}\ Cr' + \textbf{0.0634}\ Co'$$
$$-\textbf{0.4023}\ Mo' - \textbf{0.2251}\ Re'$$

with $R^2_{adj} = 98.2\%$ and rmsE = 0.0233% (12)

where the lattice mismatch is in percent and the terms that are followed by prime signs are the same as those defined for Equation (1). The regression analysis indicated that Cr, Mo, and Re drove the lattice mismatch in the negative direction, with Mo having the biggest overall effect over its entire compositional range. These compositional effects are clearly seen in the regression model output curves in Figures 24(a) and (c). In contrast, Co pushed the lattice mismatch in the positive direction and had the smallest impact, which is evident in the model output curves in Figure 24(b).
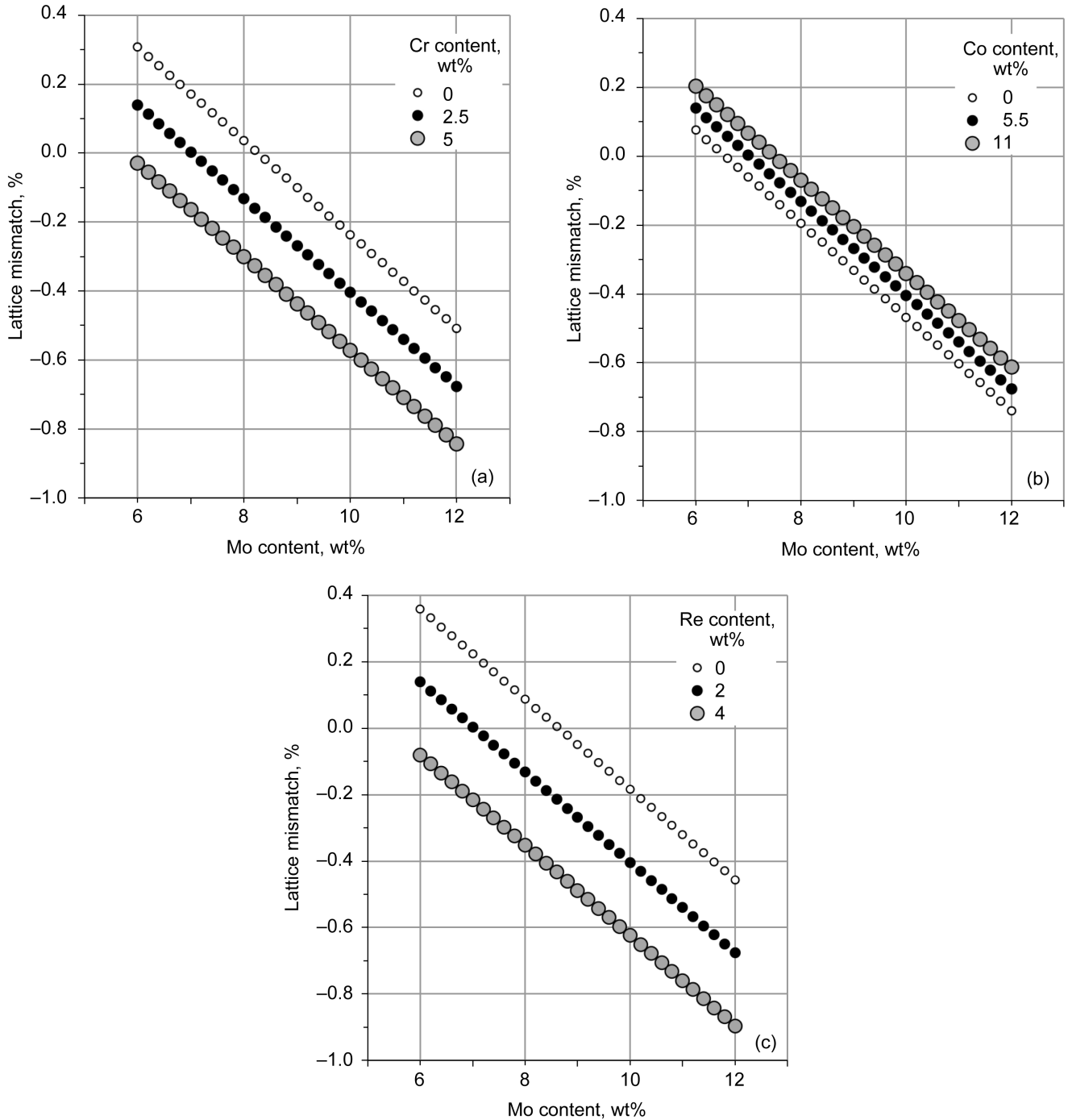

Figure 24.—Regression model output curves for estimated γ-γ' lattice mismatch at room temperature as a function of bulk Mo content. (a) 0, 2.5, and 5 wt% Cr, with Co and Re fixed at their midrange levels. (b) 0, 5.5, and 11 wt% Co, with Cr and Re fixed at their midrange levels. (c) 0, 2, and 4 wt% Re, with Cr and Co fixed at their midrange levels.
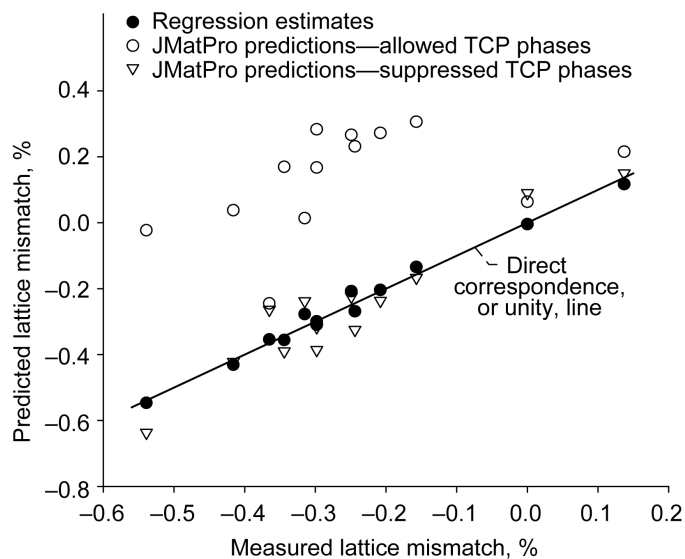
Figure 25.—Excellent fit of the linear regression model developed in this study is shown by the closed symbols for the measured g‑g¢ lattice mismatch. The model fits the LDS alloys exhibiting positive and near zero values of mismatch, as well as negative values of mismatch. JMatPro predictions of lattice mismatch are shown for the case in which all topologically closed-packed (TCP) phases were allowed to precipitate and for the case in which TCP phases were suppressed.

The regression model for lattice mismatch provided an excellent fit for alloys having positive, near zero, or negative values of lattice mismatch, which is shown by the solid symbols in Figure 25. In contrast, the open circles near the top of the figure demonstrate that JMatPro predicted a majority of the alloys to have positive values of lattice mismatch, which was not observed experimentally (Table VI). This discrepancy was very significant, with JMatPro predicting mismatch values an average of 0.48% higher than the experimentally determined values. If selections were made within the software program to suppress TCP phase formation, the JMatPro predictions for g‑g¢ lattice mismatch moved closer to the experimentally determined values, as seen in Table VI and by the open triangles in Figure 25.

Discussion

Element Potency Effects on Microstructural Parameters

The statistical regression models generated in this study provided excellent estimates of the microstructural parameters based on bulk alloy composition and demonstrate the usefulness of such formulas. Standardizing the regression coefficients over the element's compositional range made it possible to compare the *relative effects* of each significant term in the equations *over the entire compositional range varied for that element*. Clearly, the impact of Co and Cr as

g¢ solvus depressants was in agreement with previous investigations (Refs. 4 to 6 and 14). Re and Mo were found to increase the g¢ solvus. The effects of composition on g¢ volume fraction were similar to the effects of composition on g¢ solvus, which was not surprising since empirical measurements of g¢ solvus and high-temperature g¢ volume fraction tend to correlate (Refs. 4, 5, 14, and 18).

An alternative way to examine compositional effects on microstructural responses is to consider an element's potency, which is defined on a per atomic percent basis by dividing the change of a microstructural parameter by the bulk compositional range of an element in atomic percent over which that change occurred. The potency of each element was calculated for each microstructural parameter investigated because some elements may have produced a large effect through being varied over a wide content range. For example, Co was shown to decrease the g¢ solvus temperature in Equation (1) by a very significant ‑46.2 °C over its wide 11.1 at% range, yet this corresponded to a change of only ‑4.1 °C/at% Co. Cr had an equivalent potency at ‑4.1 °C/at% Cr, and Mo displayed a weak potency on g¢ solvus at +2.5 °C/at% Mo. However, Re increased the g¢ solvus by +14.3 °C/at% Re. Therefore, although Co produced the largest change in g¢ solvus over its wide compositional range, on a per atomic percent basis, Re was the most potent in producing a change in the g¢ solvus.

Re also was found to be the most potent element affecting the g¢ volume fraction at 982 °C—increasing this parameter +2.3 vol%/at% Re. Mo had a high potency as well—increasing this parameter +1.9 vol%/at% Mo. In contrast, Cr and Co decreased the g¢ volume fraction at 982 °C by ‑0.26 and ‑0.19 vol%/at%, respectively. In addition, Re did not have a statistically significant influence on the g¢ volume fraction at 1093 °C. This was particularly surprising since Re had such a potent effect on g¢ volume fraction at 982 °C. At 1093 °C, Mo produced the most potent effect on the g¢ volume fraction at +0.99 vol%/at% Mo. Cr was slightly less potent at ‑0.89 vol%/at% Cr, and Co was weaker at ‑0.34 vol%/at% Co.

Re once again was shown to be a very potent alloying element with respect to its effect on the g lattice parameter, even with the inclusion of a negative MoRe interaction term. The interaction term produced nonparallel model output curves for the g lattice parameter for Re levels as a function of Mo, and thus the potency of Re was influenced by the amount of Mo in the alloy and vice versa. The potency of Re on the g lattice parameter ranged from a low of 0.0101 Å/at% Re at the highest bulk Mo content to a high of 0.0141 Å/at% Re at the lowest Mo content in the bulk. Mo's highest potency level was found to be 0.0089 Å/at% Mo in the absence of Re and was 0.0075 Å/at% Mo at the highest bulk Re content. Thus, both Re and Mo were more potent when the other element either was not present or was present at lower levels. In contrast, Cr was not nearly as potent of an alloying element on the g lattice parameter at +0.0023 Å/at% Cr, and Co was even less effective at ‑0.0004 Å/at% Co. The same ranking of

the potency of these elements was observed for γ-γ′ lattice mismatch, which would be expected because the γ′ lattice parameters did not change much, whereas the γ lattice parameters demonstrated a strong compositional dependence. Re was found to be the most potent alloying element since it changed mismatch by −0.336 %Δ/at% Re. The potency of Mo ranked second at −0.222 %Δ/at% Mo. In contrast, Cr at −0.059 %Δ/at% Cr and Co at +0.011 %Δ/at% Co were less effective. The influences of these elements on the γ lattice parameter may be explained by their atomic size, as well as by their influence on the resulting γ phase chemistry, which is explained in the following section.

γ and γ′ Phase Chemistries

The γ and γ′ phase chemistries exhibited some interesting temperature dependencies that were strongly influenced by the temperature dependency of the γ′ volume fraction. More γ′ (and therefore less γ) was present at 871 °C than at 1093 °C; thus, the γ formers were more heavily concentrated in the γ phase at the lower aging temperatures. As the temperature increased, the elements that were tied up in the γ′ phase dissolved into the γ matrix, and this resultant effect was seen in the measured γ phase chemistries. The Cr, Co, Mo, and Re concentrations in the γ′ phase were much more constant as a function of temperature, although small but consistent changes were observed (Figs. 15(a) to (d)). The concentration of γ formers in the γ′ phase increased slightly as the temperature increased and the γ′ volume fraction decreased. However, the Mo level in γ′ was an exception to this trend because its concentration decreased with increasing temperature, as seen in Figure 15(c). This decrease may have been the result of limited solubility of Mo in the γ′ phase with increasing temperature (Ref. 11), particularly in the presence of a strong γ′ former such as Ta. Loomis et al. (Ref. 11) reported similar trends and small changes in magnitude of the Cr, Al, and Mo concentrations in the γ′ phase of Ni-Al-Mo-Cr alloys as aging temperature increased, and noted that Ti sharply reduced Mo solubility in the γ′ phase. It seems quite possible that Ta behaves similarly to Ti in reducing the solubility of Mo in γ′ with increasing temperature.

One may rationalize the relative magnitudes of the coefficients in the γ lattice parameter regression equation on the basis of atomic radii. The elements with an atomic radius closer to that of Ni would be expected to have a smaller effect on the γ lattice parameter and smaller regression coefficients in Equation (10). Clearly Co and Cr have smaller atomic sizes (Ref. 38) and smaller regression coefficients relative to Mo and Re. In addition, the regressions showing the effects of bulk chemistry changes on the γ phase chemistries help to further explain the γ lattice parameters, since changes in the bulk chemistry of one γ former often affected the concentrations of other elements in the γ phase. The phase chemistries at 871 °C were pertinent to this discussion because this was the last aging step before lattice parameter

measurements were obtained at room temperature. For example, from Equation 4(a) and (c), as Cr was increased in the bulk from 2.8 to 5.7 at% with the other γ formers held constant at their midrange levels, the concentrations of Cr and Mo in the γ phase increased significantly from 5.6 to 14.1 at% Cr and from 7.4 to 8.9 at% Mo. These effects of Cr would both increase the γ lattice parameter and drive the γ-γ′ lattice mismatch in the negative direction. Similarly, as Mo in the bulk was increased, the concentrations of both Mo and Cr increased in the γ phase. These effects of Mo also would serve to amplify the increase in γ lattice parameter and drive the lattice mismatch in the negative direction.

Although Mo has a slightly larger atomic radius than Re (Ref. 38), increasing Re in the bulk alloy increased the concentrations of Re, Cr, and Co in the γ phase at 871 °C. This overall effect of Re would cause an increase in the γ lattice parameter and would also drive the lattice mismatch in the negative direction. Co was the only alloying element in this study that both partitioned to the γ phase, and based on Equation (10) and Figure 23(b), decreased the γ lattice parameter, which would drive the mismatch in a slightly positive direction. This effect of Co has also been observed in first-generation single crystal alloys (Refs. 4 and 5). In contrast, Caron (Ref. 14) indicated that Co increased the γ lattice parameter in superalloys, based on calculated γ lattice parameters that used the lattice parameters of pure Ni and Ni-Co binaries, as well as calculated γ compositions. In the present study, adding Co to the bulk alloy significantly increased the amount of Co in the γ and γ′ phases and had a small effect in decreasing the Ta concentration in the γ phase. Co had no effect on the concentration of any other γ former at 871 °C. The negative effect of Co on the γ lattice parameter cannot be rationalized on the basis of atomic size or Ni-Co binary data. It can only be ventured that the Co effect is quite small and is the consequence of subtle changes in phase chemistries.

Topologically Close-Packed Phases

The qualitative trends in TCP phase formation as a function of composition were not unexpected because it is well known that increasing the refractory metal content increases the propensity for TCP formation. This is consistent with the EDS analysis performed in this study on extracted TCP precipitates, which showed that the TCP laths were rich in Mo, Ni, Re, and to a lesser extent, Cr. One key to successful alloy development is to know with very high accuracy the critical concentration limits for the strengthening elements and for the critical combination of elements. PHACOMP (Ref. 28) and M_d (Ref. 29) results did not provide a clear limit for the concentration of refractories in LDS composition space, and another study (Ref. 39) agrees that they are not robust predictors of TCP formation. Knowledge of the γ phase chemistry as a function of temperature may be used to update and improve N_{v3} equations for a set of alloys. However, within

this alloy design space, the total refractory metal (Cr + Mo + Re) content in the bulk alloy provided a useful tool for predicting the influence of alloying on third phase precipitation since this approach revealed a critical refractory metal content of 15.3 wt%, above which excessive TCP phase precipitation was induced.

Any additional conclusions based on compositional effects on TCP formation are provisional in nature because most of the LDS alloys were stable. Only two alloys exhibited TCP volume fractions significantly greater than 1 vol%, and more unstable alloys would need to be examined to capture with more certainty the compositional effects on this microstructural parameter. Co is of particular interest since it was intentionally varied in this design space because of its reported benefit in reducing TCP content (Refs. 4 to 6, 30, and 32). Comparison of the TCP contents in LDS–1101 and LDS–1501 is consistent with that trend, although the TCP content in both of these alloys was low (<1 vol%). Similarly, LDS–4183 and LDS–4583 showed a small beneficial effect of Co at 1093 °C, although at 982 °C, their mean third phase volume fractions were not statistically different. Table III demonstrates that JMatPro predicted Co to have a detrimental effect on TCP precipitation at 982 °C, although it predicted a beneficial effect at 1093 °C. PHACOMP and M_d also did not predict the beneficial effect of Co on microstructural stability, but instead predicted the opposite.

The exact mechanism for the potential beneficial effect of Co in reducing TCP content is still open for discussion. One possible mechanism is that Co may increase the solubility of refractory metals in the γ and γ′ phases (Ref. 5), thereby increasing the saturation limits and reducing supersaturation of the refractories in the γ phase. Another mechanism postulated (Refs. 6 and 32) is that Co may change the partitioning ratio of alloying elements by forcing higher quantities of the γ formers into the γ′ phase, thereby diluting the refractories in the γ phase. This idea was not supported in the present study by the regressions of the phase chemistries obtained between 871 and 1093 °C. Another plausible mechanism is that Co may reduce the supersaturation of refractory metals in the γ matrix directly by decreasing the γ′ volume fraction and increasing the γ volume fraction, thereby diluting the refractories in the γ phase. Other factors believed to be important in affecting stability include the individual character and potency of each alloying element, plus the presence or absence of other elements.

It should be noted that prior work (Refs. 2 and 3) indicated higher TCP volume fractions for LDS–5051 were formed after 500 h of unstressed aging, as compared to that in the present report after creep exposures at the same temperatures. This was particularly evident at 982 °C where 6.1 vol% of third phase was measured after aging (Refs. 2 and 3), compared with 0.3 vol% of third phase obtained after creep exposures. At 1093 °C, 4.1 vol% of third phase was measured in LDS–5051 after aging (Refs. 2 and 3), and 2.4 vol% of third phase was observed after creep exposures. The other LDS alloys without the Hf addition showed no significant

differences in third phase content between stressed and unstressed exposures, with all quantities being £1 vol%. However, the Hf-bearing alloys seemed more prone to measurable differences between types of exposures, although these differences were not nearly as dramatic as those observed for LDS–5051. The Hf-bearing alloys exhibited on average 1 vol% more third phase after aging at 982 °C than after creep at 982 °C, and they exhibited on average 0.7 vol% more third phase after aging at 1093 °C than after creep at 1093 °C. Some studies (Refs. 26 and 40) concluded that the application of stress decreases the amount of TCP phase precipitation in single crystals during high-temperature exposures. This is worthy of further investigation since screening for microstructural stability is usually done via unstressed aging, despite service conditions being under applied stress at elevated temperatures.

Comparisons to Computational Tool Predictions

Software tools that use computational thermodynamics are of growing importance and are commonly used to predict various microstructural parameters in Ni-base superalloys. However, major discrepancies were observed between computational tool predictions and the experimental data generated in this study. JMatPro significantly underpredicted both the γ′ solvus (by an average of 10 °C) and the solidus (by an average of 17 °C). If these predictions are used in practice and in the absence of experimental data, heat treatment temperatures could be far from optimum, resulting in unsolutioned primary γ′ Furthermore, with JMatPro the combination of the lower solvus temperature predictions and even lower solidus temperature predictions serves to predict unrealistically small heat treatment windows, which could eliminate viable alloys from adequate consideration. JMatPro also underpredicted the quantity of γ′ by an average of 10 vol% at 1093 °C. Since γ′ is the strengthening precipitate in Ni-base superalloys, use of such predictions in alloy development could cause an unnecessary redesign of the composition space. Therefore, improvement in the predictive capabilities of these computational thermodynamic modeling tools should be a high priority.

JMatPro predicted the LDS alloys to have positive γ-γ′ lattice mismatches so large in magnitude at room temperature that if these predictions were accurate, many of the alloys in this study would be expected to have positive mismatch also at creep-testing temperatures. In Ni-base superalloys, the thermal expansion coefficient of the γ′ phase is typically smaller than that of the γ matrix (Ref. 34). Thus, as temperature is increased, the lattice parameter of the γ phase increases more than that of the γ′ phase. However, empirical results from high-temperature x-ray diffraction show that the magnitude of the lattice mismatch in Ni-base superalloys changes only by a small amount from the room temperature measurements. For example, a change in the magnitude of lattice mismatch of no more than 0.1% was measured in Re-free alloys from room temperature to 1000 °C (Ref. 34), and alloys with higher

refractory metal content were noted to exhibit lower thermal expansion coefficients for both the γ and γ' phases. Other studies (Ref. 41) showed a change in the magnitude of lattice mismatch of up to 0.2% in Re-free alloys and up to 0.12% in Re-bearing alloys from room temperature to 1000 °C. Alloys that have positive lattice mismatch at elevated temperatures produce γ' rafts that align parallel to the applied stress direction during creep exposures (Refs. 34 and 42). However, as seen in the photomicrographs in Figures 4 to 5, all LDS alloys in this study developed rafts perpendicular to the applied stress direction during creep testing, which is expected for alloys with negative mismatch at elevated temperatures. Thus, many of the JMatPro predictions for lattice mismatch were not only of the wrong sign at room temperature, but many were expected to be too large in magnitude to become negative at creep-testing temperatures. Neither the empirically determined mismatch values, nor the microstructural evidence for the sign of lattice mismatch at elevated temperatures in this study, support the JMatPro predictions for γ-γ' mismatch.

User selections within the JMatPro program greatly affected the predictions of lattice mismatch, and users clearly need to be cognizant of such options. Because JMatPro overpredicted the amount of TCP observed experimentally in this study, it seemed logical to try to suppress TCP formation within the software and examine its effects on predicted lattice parameters. This approach dramatically improved the software's predictions for γ lattice parameters at room temperature (Table VI), but it resulted in a slight, concurrent worsening of γ' lattice parameter predictions. Additionally, the selection of a heat treatment temperature range within the software greatly impacted the predictions.

JMatPro predicted the carbide types that were identified experimentally by x-ray diffraction in the present alloys. Other investigators (Ref. 43) also concluded that the thermodynamic calculations usually predict the correct carbides. However, JMatPro did a less than satisfactory job in predicting the presence and amount of third phases in the LDS composition space, and this was consistent with other observations (Refs. 39, 43, and 44). Specifically, in this study it was found that JMatPro significantly overpredicted the amount of third phase precipitates observed at 982 °C and predicted 10 out of 14 alloys to be unstable when they were in fact stable (Table III). Alternatively, at 1093 °C JMatPro predicted that all LDS alloys were stable, including the two LDS alloys that were unstable. One reason that is given for such discrepancies is that some of the TCP phases are poorly described within the thermodynamic database because experimental data are often scarce (Ref. 39). Furthermore, a criticism of validation testing is that the experimental results do not represent the equilibrium conditions that the thermodynamic calculations are predicting (Ref. 43) in software packages such as JMatPro. Because the amount of third phase precipitates did not change significantly after 200 h of creep exposure, the authors believe that the experimental results in this study represent near-equilibrium conditions for the third phases, and thus the observed discrepancy between experimental results and JMatPro predictions cannot be explained by the absence of equilibrium conditions. The authors hope that the experimental results described herein can be used to improve the predictive capabilities of these physics-based computational tools.

Conclusions

1. Regression models developed in the present study fit the γ' solvus, γ' volume fraction, γ lattice parameter, and γ-γ' lattice mismatch extremely well and demonstrated the usefulness of such methods for estimating bulk compositional effects.

2. Co decreased γ' solvus temperatures and had the biggest impact on this parameter over its 0 to 11 wt% range. Mo had the biggest influence over its 6 to 12 wt% range on increasing the γ lattice parameter and the magnitude of γ-γ' lattice mismatch. Co and Cr decreased γ' volume fraction, but Mo and Re increased γ' volume fraction. However, for the microstructural parameters examined, Re was the most potent alloying element investigated on an atomic percent basis.

3. Refractory metal concentration limits that avoid excessive topologically close-packed (TCP) phase formation were best described by the total Cr + Mo + Re content in the bulk alloy. PHACOMP and the critical value based on the d-electrons concept M_d were less effective discriminators.

4. Re, Cr, Mo, and Co preferentially partitioned to the γ phase, although they also exhibited some solubility in the γ' phase. Partitioning and phase chemistries were not constant but were a function of temperature and bulk alloy composition.

5. Phase chemistry changes were affected by the decrease in γ' volume fraction with increasing temperature. The γ phase exhibited large compositional changes with temperature; the γ' chemistry exhibited some very small, but consistent changes, as a function of temperature.

6. JMatPro correctly identified the observed carbide type in the low-density single crystal (LDS) alloys and provided reasonably close estimations of the γ' lattice parameters. However, JMatPro underestimated the γ' volume fraction and the γ' solvus, the latter of which could lead to the use of inadequate heat treatment temperatures that do not fully solution the primary γ' phase, thereby negatively impacting mechanical properties.

7. JMatPro tended to grossly overpredict the amount of TCP phase that actually formed. However, its predictions for γ lattice parameters and γ-γ' lattice mismatch could be improved if TCP phase precipitation was suspended in the software program.

References

1. MacKay, Rebecca A., et al.: Low Density, High Creep Resistant Single Crystal Superalloy for Turbine Airfoils. U.S. Patent 7,261,783 B1, Aug. 2007.

2. MacKay, Rebecca A., et al.: Alloy Design Challenge: Development of Low Density Superalloys for Turbine Blade Applications. NASA/TM—2009-215819, 2009. http://ntrs.nasa.gov

3. MacKay, R.A., et al.: A New Approach of Designing Superalloys for Low Density. JOM, vol. 62, no. 1, 2010, pp. 48–54.

4. Nathal, Michael V.: Influence of Cobalt, Tantalum, and Tungsten on the High Temperature Mechanical Properties of Single Crystal Nickel-Base Superalloys. NASA TM–83479, 1984. http://ntrs.nasa.gov

5. Nathal, M.V.; and Ebert, L.J.: The Influence of Cobalt, Tantalum, and Tungsten on the Microstructure of Single Crystal Nickel-Base Superalloys. Metall. Trans. A, vol. 16, no. 10, 1985, pp. 1849–1862.

6. Walston, S., et al.: Joint Development of a Fourth Generation Single Crystal Superalloy. Superalloys 2004 (NASA/TM—2004-213062), K.A. Green et al., eds., TMS, Warrendale, PA, 2006, pp. 15–25.

7. Wang, W.Z., et al.: Role of Re and Co on Microstructures and γ¢ Coarsening in Single Crystal Superalloys. Mater. Sci. Eng. A, vol. 479, 2008, pp. 148–156.

8. MacKay, R.A.; and Ebert, L.J.: Factors Which Influence Directional Coarsening of γ¢ During Creep in Nickel-Base Superalloy Single Crystals. Superalloys 1984, M. Gell et al., eds., TMS, Warrendale, PA, 1984, pp. 135–144.

9. MacKay, R.A.; Nathal, M.V.; and Pearson, D.D.: Influence of Molybdenum on the Creep Properties of Nickel-Base Superalloy Single Crystals. Metall. Trans. A, vol. 21A, 1990, pp. 381–388.

10. MacKay, R.A.; and Nathal, M.V.: γ¢ Coarsening in High Volume Fraction Nickel-Base Alloys. Acta Metall. Mater., vol. 38, no. 6, 1990, pp. 993–1005.

11. Loomis, W.T.; Freeman, J.W.; and Sponseller, D.L.: The Influence of Molybdenum on the g¢ Phase in Experimental Nickel-Base Superalloys. Metall. Trans., vol. 3, 1972, pp. 989–1010.

12. Miller, R.F.; and Ansell, G.S.: Low Temperature Mechanical Behavior of Ni-15Cr-Al-Ti-Mo Alloys. Metall. Trans. A, vol. 8A, 1977, pp. 1979–1998.

13. Grose, D.A.; and Ansell, G.S.: The Influence of Coherency Strain on the Elevated Temperature Tensile Behavior of Ni-15Cr-Al-Ti-Mo Alloys. Metall. Trans. A, vol. 12A, 1981, pp. 1631–1645.

14. Caron, P.: High g¢ Solvus New Generation Nickel-Based Superalloys for Single Crystal Turbine Blade Applications. Superalloys 2000, K.A. Green, Tresa M. Pollock, and Robert D. Kissinger, eds., TMS, Warrendale, PA, 2000, pp. 737–946.

15. Saunders, N., et al.: Using *JMatPro* to Model Materials Properties and Behavior. JOM, vol. 55, no. 12, 2003, pp. 60–65.

16. Saunders, N., et al.: Modelling the Material Properties and Behaviour of Ni-Based Superalloys. Superalloys 2004, K.A. Green et al., eds., TMS, Warrendale, PA, 2004, pp. 849–858.

17. Donachie, Matthew J.; and Donachie, Stephen J.: Superalloys: A Technical Guide, Second ed., ASM International, Materials Park, OH, 2002.

18. Kriege, O.H.; and Baris, J.M.: The Chemical Partitioning of Elements in γ¢ Separated From Precipitation-Hardened, High-Temperature Nickel-Base Alloys. ASM Trans. Quart., vol. 62, 1969, pp. 195–200.

19. Reed, Roger C.: The Superalloys: Fundamentals and Applications. Cambridge University Press, Cambridge, UK, 2006, pp. 148-170.

20. Burton, C.J.: Differential Thermal Analysis and the Mechanisms of Minor Additions in Superalloys. Superalloys 1976, B.H. Kear, ed., TMS, Warrendale, PA, 1976, pp. 147–158.

21. Sponseller, D.L.: Differential Thermal Analysis of Nickel-Base Superalloys. Superalloys 1996, R.D. Kissinger, ed., TMS, Warrendale, PA, 1996, pp. 259–270.

22. Pearson, D.D.; Lemkey, F.D.; and Kear, B.H.: Stress Coarsening of g¢ and Its Influence on Creep Properties of a Single Crystal Superalloy. Superalloys 1980, J.K. Tien et al., eds., TMS, Warrendale, PA, 1980, pp. 513–520.

23. Pearson, D.D.; Kear, B.H.; and Lemkey, F.D.: Factors Controlling the Creep Behavior of a Nickel-Base Superalloy. Creep and Fracture of Engineering Materials and Structures, B. Wilshire and D.R.J. Owens, eds., Pineridge Press, Swansea, UK, 1981, pp. 213–233.

24. MacKay, Rebecca A.; and Ebert, Lynn J.: The Development of Directional Coarsening of the g¢ Precipitate in Superalloy Single Crystals. Scr. Metall., vol. 17, no. 10, 1983, pp. 1217–1222.

25. MacKay, Rebecca A.; and Nathal, Michael V.: Microstructure-Property Relationships in Directionally Solidified Single-Crystal Nickel-Base Superalloys. MiCon 86: Optimization of Processing, Properties, and Service Performance Through Microstructural Control, ASTM STP 979, B.L. Bramfitt et al., eds., 1988, pp. 202–221.

26. Pessah, M.; Caron, P.; and Khan, T.: Effect of m Phase on the Mechanical Properties of a Nickel-Base Single Crystal Superalloy. Superalloys 1992, S.D. Antolovich et al., eds., TMS, Warrendale, PA, 1992, pp. 567–576.

27. Darolia, R., et al.: Formation of Topologically Closed Packed Phases in Nickel Base Single Crystal Superalloys. Superalloys 1988, D.N. Duhl et al., eds., TMS, Warrendale, PA, 1988, pp. 255–264.

28. Wlodek, S.T.: The Stability of Superalloys. Long Term Stability of High Temperature Materials, G.E. Fuchs, K.A. Dannemann, and T.C. Deragon, eds., TMS, Warrendale, PA, 1999, pp. 1–40.

29. Morinaga, M., et al.: New PHACOMP and Its Applications to Alloys Design. Superalloys 1984, M. Gell et al., eds., TMS, Warrendale, PA, 1984, pp. 523–532.

30. O'Hara, Kevin S., et al.: Nickel Base Superalloy and Article. U.S. Patent 5,482,789, Jan. 1996.

31. Dreshfield, Robert L.; and Thomas, Kimberly J.: Analyses of Elemental Partitioning in Advanced Nickel-Base Superalloy Single Crystals. NASA/TM—2005-213288, 2005. Available from the NASA Center for Aerospace Information.

32. Rae, C.M.F.; and Reed, R.C.: The Precipitation of Topologically Close-Packed Phases in Rhenium-Containing Superalloys. Acta Mater., vol. 49, 2001, pp. 4113–4125.

33. Reed, R.C., et al.: Identification of the Partitioning Characteristics of Ruthenium in Single Crystal Superalloys Using Atom Probe Tomography. Scr. Mater., vol. 51, 2004, pp. 327–331.

34. Nathal, M.V.; MacKay, R.A.; and Garlick, R.G.: Temperature Dependence of γ-γ' Lattice Mismatch in Nickel-Base Superalloys. Mater. Sci. Eng., vol. 75, 1985, pp. 195–205.

35. Nathal, M.V.; MacKay, R.A.; and Garlick, R.G.: Lattice Parameter Variations During Aging in Nickel-Base Superalloys. Scr. Metall., vol. 22, 1988, pp. 1421–1424.

36. Lasalmonie, A.; and Strudel, J.L.: Interfacial Dislocation Networks Around γ' Precipitates in Nickel-Base Alloys. Phil. Mag., vol. 32, no. 5, 1975, pp. 937–949.

37. Nathal, M.V.; MacKay, R.A.; and Garlick, R.G.: Erratum in Mater. Sci. Eng., vol. 80, 1986, p. 101.

38. Clementi, E.; Raimondi, D.L.; and Reinhardt, W.P.: Atomic Screening Constants From SCF Functions. II. Atoms With 37 to 86 Electrons. J. Chem. Phys., vol. 47, no. 4, 1967, pp. 1300–1307.

39. Seiser, B.; Drautz, R.; and Pettifor, D.G.: TCP Phase Predictions in Ni-Based Superalloys: Structure Maps Revisited. Acta Mater., vol. 59, 2011, pp. 749–763.

40. Acharya, M.V.; and Fuchs, G.E.: The Effect of Stress on the Microstructural Stability of CMSX–10 Single Crystal Ni-Base Superalloys. Scr. Mater., vol. 54, 2006, pp. 61–64.

41. Pyczak, F.; Devrient, B.; and Mughrabi, H.: The Effects of Different Alloying Elements on the Thermal Expansion Coefficients, Lattice Constant and Misfit of Nickel-Based Superalloys Investigated by X-ray Diffraction. Superalloys 2004, K.A. Green et al., eds., TMS, Warrendale, PA, 2004, pp. 827–836.

42. Gayda, J.; and MacKay, R.A.: Analysis of γ' Shape Changes in a Single Crystal Ni-Base Superalloy. Scr. Metall., vol. 23, 1989, pp. 1835–1838.

43. Zhao, J.-C.; and Henry, M.F.: CALPHAD—Is It Ready for Superalloy Design? Adv. Eng. Mat., vol. 4, no. 7, 2002, pp. 501–508.

44. Copland, Evan H.; Jacobson, Nathan S.; and Ritzert, Frank J.: Computational Thermodynamic Study to Predict Complex Phase Equilibria in the Nickel-Base Superalloy René N6. NASA/TM—2001-210897, 2001.

1. REPORT DATE *(DD-MM-YYYY)* 01-10-2012	2. REPORT TYPE Technical Paper	3. DATES COVERED *(From - To)*

4. TITLE AND SUBTITLE Compositional Effects on Nickel-Base Superalloy Single Crystal Microstructures	5a. CONTRACT NUMBER
	5b. GRANT NUMBER
	5c. PROGRAM ELEMENT NUMBER
6. AUTHOR(S) MacKay, Rebecca, A.; Gabb, Timothy, P.; Garg, Anita; Rogers, Richard, B.; Nathal, Michael, V.	5d. PROJECT NUMBER
	5e. TASK NUMBER
	5f. WORK UNIT NUMBER WBS 561581.02.08.03.47.01.01

7. PERFORMING ORGANIZATION NAME(S) AND ADDRESS(ES) National Aeronautics and Space Administration John H. Glenn Research Center at Lewis Field Cleveland, Ohio 44135-3191	8. PERFORMING ORGANIZATION REPORT NUMBER E-18091-1

9. SPONSORING/MONITORING AGENCY NAME(S) AND ADDRESS(ES) National Aeronautics and Space Administration Washington, DC 20546-0001	10. SPONSORING/MONITOR'S ACRONYM(S) NASA
	11. SPONSORING/MONITORING REPORT NUMBER NASA/TP-2012-217626

12. DISTRIBUTION/AVAILABILITY STATEMENT
Unclassified-Unlimited
Subject Category: 26
Available electronically at http://www.sti.nasa.gov
This publication is available from the NASA Center for AeroSpace Information, 443-757-5802

13. SUPPLEMENTARY NOTES

14. ABSTRACT
Fourteen nickel-base superalloy single crystals containing 0 to 5 wt% chromium (Cr), 0 to 11 wt% cobalt (Co), 6 to 12 wt% molybdenum (Mo), 0 to 4 wt% rhenium (Re), and fixed amounts of aluminum (Al) and tantalum (Ta) were examined to determine the effect of bulk composition on basic microstructural parameters, including γ' solvus, γ' volume fraction, volume fraction of topologically close-packed (TCP) phases, phase chemistries, and γ - γ' lattice mismatch. Regression models were developed to describe the influence of bulk alloy composition on the microstructural parameters and were compared to predictions by a commercially available software tool that used computational thermodynamics. Co produced the largest change in γ' solvus over the wide compositional range used in this study, and Mo produced the largest effect on the γ lattice parameter and the γ - γ' lattice mismatch over its compositional range, although Re had a very potent influence on all microstructural parameters investigated. Changing the Cr, Co, Mo, and Re contents in the bulk alloy had a significant impact on their concentrations in the γ matrix and, to a smaller extent, in the γ' phase. The γ phase chemistries exhibited strong temperature dependencies that were influenced by the γ and γ' volume fractions. A computational thermodynamic modeling tool significantly underpredicted γ' solvus temperatures and grossly overpredicted the amount of TCP phase at 982 °C. Furthermore, the predictions by the software tool for the γ - γ' lattice mismatch were typically of the wrong sign and magnitude, but predictions could be improved if TCP formation was suspended within the software program. However, the statistical regression models provided excellent estimations of the microstructural parameters based on bulk alloy composition, thereby demonstrating their usefulness.

15. SUBJECT TERMS
Superalloy; Microstructure; Gamma prime; Composition; Lattice parameter; Regression; Computational modeling; Topologically close packed phase; X-ray diffraction; Lattice mismatch; Solvus; Nickel

16. SECURITY CLASSIFICATION OF:			17. LIMITATION OF ABSTRACT	18. NUMBER OF PAGES	19a. NAME OF RESPONSIBLE PERSON STI Help Desk (email:help@sti.nasa.gov)
a. REPORT U	b. ABSTRACT U	c. THIS PAGE U	UU	42	19b. TELEPHONE NUMBER *(include area code)* 443-757-5802